

# Using Simulations to Guide the Design of Amperometric Electrochemical Sensors Based on Mediated Electron Transfer

Joseph R. Elliott, Haonan Le, Minjun Yang, and Richard G. Compton<sup>\*,[a]</sup>

Mediated electron-transfer sensors provide a practical means of detection for species for whom direct electron-transfer sensors are impractical. Through the use of numerical simulation, the design and optimisation of mediated electron-transfer sensors are presented in this work where we specifically consider the mediation as an irreversible process. Comparison is made between sensors employing the mediator as an adsorbed monolayer on the electrode's surface and sensors employing it as a soluble additive to the sample, with the former being

concluded as preferable due to improved detection limits and practicality. Studies are performed for the optimisation of the electrode radius, mediating chemical rate constant and scan rate, with consideration also given to the capacitive current. Triangular and semi-circular sweep voltammetry are compared in the context of mediating electron-transfer sensor design. It is concluded that competition between the Faradaic and capacitive currents is a primary limitation for this technique.

## 1. Introduction

Amperometric electrochemical sensors can offer merits which include sensitivity, low cost, ease of use and sometimes selectivity<sup>[1–4]</sup> in comparison with alternative approaches including potentiometric electrochemical sensors. Accordingly they have developed so as to occupy a niche area in the chemical sensors arena with conspicuous success, for example, in their application to the sensing of glucose in blood<sup>[5,6]</sup> and in gas sensing<sup>[7]</sup> such as those employed in fire alarms and smoke detectors for the sensing of carbon monoxide. A wide range of amperometric gas sensors are available commercially.<sup>[8–11]</sup> Other areas of conspicuous commercial success include enzyme-based biosensors<sup>[12–14]</sup> and amperometric approaches to pH.<sup>[15–17]</sup>

In some applications the direct electrolysis of the analyte,  $X$ , can be used to generate a current which is proportional to the concentration to be measured where the maximum rate of the reaction,  $X \pm ne^- \rightleftharpoons \text{products}$ , reflects the rate of mass transport, usually pre-dominantly diffusion, to the electrode surface. Thus, for a micro-disc electrode of radius  $r$ , the steady-state diffusion-controlled current is given by Equation (1):<sup>[18,19]</sup>

$$I = 4nFD_X[X]_{\text{bulk}}r_e \quad (1)$$

where  $r_e$  is the radius of the microdisc electrode,  $n$  is the number of electrons transferred,  $F$  is the Faraday constant,  $[X]_{\text{bulk}}$  is the initial concentration of the analyte  $X$ , and  $D_X$  is the diffusion coefficient of  $X$ . For a spherical counterpart, the steady-state current is Equation (2).<sup>[20]</sup>


$$I = 4\pi nFD_X[X]_{\text{bulk}}r_e \quad (2)$$

For a macro-electrode experiencing diffusion control then at short times the current is given by the Cottrell equation [Eq. (3)].<sup>[21]</sup>

$$I = nFAc^* \sqrt{\frac{D}{\pi t}} \quad (3)$$

where  $t$  is the time from the start of the diffusion-controlled electrolysis. However rather than decreasing to zero as predicted by Equation (3) as time extends beyond ca. 10 s of seconds of electrolysis, experiment shows that an approximately steady current is reached, the magnitude of which is again proportional to the concentration of  $X$  but which also reflects the extent of the so-called 'natural convection' in the vicinity of the electrode. The latter is induced by density differences, asserted by Levich to be the exclusive cause.<sup>[22]</sup> The latter can be driven by temperature gradients which in turn are most notably caused by evaporative losses from liquid surfaces.<sup>[23,24]</sup> Such natural convection currents are likely to be to some extent unreproducible unless the supply of analyte to the macroelectrode surface is controlled for example as in a gas sensor where the flux through a gas permeable membrane can control the current.<sup>[7]</sup> Also mitigating in some circumstances against the use of macro-electrodes for optimal signal to background currents is the fact that the electrode capacitance scales directly with the electrode area so that for sensors in which the potential is scanned there is a relative enhancement

[a] J. R. Elliott, H. Le, M. Yang, Prof. Dr. R. G. Compton  
Department of Chemistry, Physical and Theoretical Chemistry Laboratory  
Oxford University  
South Parks Road, Oxford, OX1 3QZ, United Kingdom  
E-mail: richard.compton@chem.ox.ac.uk

 Supporting information for this article is available on the WWW under <https://doi.org/10.1002/celc.202000674>

 An invited contribution to a Special Collection on Electrochemical Sensing

© 2020 The Authors. Published by Wiley-VCH Verlag GmbH & Co. KGaA. This is an open access article under the terms of the Creative Commons Attribution License, which permits use, distribution and reproduction in any medium, provided the original work is properly cited.

of the Faradaic signal over the capacitive background as the electrode size switches from the macro- to the micro-scale corresponding to the switch from linear to convergent diffusion.

It follows from the above that if a sensor is operated under conditions of mass transport control where the applied electrode potential is sufficiently large that the electron transfer reaction is fully driven, then the current signal is likely to be largely independent of the electrode material provided that the mass transport controlled region can be accessed. An obvious exception to this arises when the nature of the products of the electrode reaction change from one electrode material to another such that different numbers of electrons ( $n$ ) are transferred. In this situation the micro-disc, Cottrellian and natural convection-controlled currents all scale with  $n$  but for linear sweep voltammetry for an electrochemically reversible couple the scaling is with  $n^{3/2}$ . An important example of where the value of  $n$  depends on the electrode material is that of the electro-reduction of di-oxygen where  $n = 2$  for carbon electrodes but  $n = 4$  for platinum. Moreover, for multi-step electrode processes involving coupled chemical kinetics (homogeneous and/or heterogeneous) changing the size of the electrode may alter the number of electrons transferred depending on the relative magnitudes of the mass transport and the chemical rates.<sup>[25]</sup> Nevertheless, for electrodes of the same geometry operating under diffusion-controlled conditions, such as chronoamperometry, the currents observed will typically be all of the same order of magnitude irrespective of the electrode material.<sup>[26]</sup>

If a sensor is operated under linear sweep voltammetry, however, the magnitude of the peak current may be enhanced for  $n > 1$  if the electrode kinetics is enhanced upon electrode modification. The ratio of the peak current between a fully reversible and a fully irreversible electrode kinetics is described by Equation (4):<sup>[26,27]</sup>

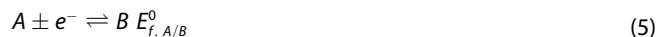
$$\frac{i_{\text{peak, reversible}}}{i_{\text{peak, irreversible}}} = 0.9 \times \frac{n^{0.5}}{(n' + \beta)^{0.5}} \quad (4)$$

where  $n'$  is the number of electrons transferred prior to the rate determining step, and  $\beta$  is the transfer coefficient. If the first electron transfer is the rate determining step, assuming  $\beta = 0.5$ , a maximum enhancement of 1.8 times in peak current for  $n = 2$  and 2.5 times for  $n = 4$  is possible.

In many cases the direct electrolysis of the analyte,  $X$ , is not possible; the heterogeneous electron transfer rate is too slow for a useful current to be obtained at potentials within the 'window' in which the solvent itself, usually but not exclusively aqueous,<sup>[28]</sup> is not oxidised or reduced. In such cases it is common to employ a mediator to facilitate the electron transfer at a convenient and practical electrode potential. One such example involves the use of the hexacyanoferrate (II/III) redox couple for the detection of hydrogen sulphide.<sup>[29]</sup> Another relates to the detection of phenols, most notably the psychoactive chemical of cannabis,  $\Delta^9$ -tetrahydrocannabinol (THC). The proof-of-concept experiments by Banks *et al.* utilised an electrogenerated product, reactive towards THC, which results

in a loss of Faradaic current during the reverse sweep proportional to the concentration of THC present.<sup>[30,31]</sup>

The present paper seeks to identify from a simulation basis, the 'best' generic approaches to the implementation of the following chemistry for the detection of the analyte  $X$  [Eqs. (5)–(7)]:



where the detection of  $C$  is used to quantify the amount of  $X$  and the potential at which  $C$  is detected is different to that of the  $A/B$  reaction, so that different voltammetric features are seen for  $A$  and for  $C$ . Note that in the scheme investigated species  $B$  is irreversibly lost by reaction with  $X$ . In particular we are interested to clarify whether the best sensitivity is obtained by immobilising the  $A/B$  couple on the electrode surface, so creating a modified electrode as pioneered by Murray,<sup>[32–34]</sup> or alternatively by deploying it dissolved in a solution phase containing  $X$ ? A second question to be addressed in this paper is whether the mediation is better implemented using a macro-electrode or a micro-electrode, noting that electrodes will have significantly different magnitudes of charging currents? Third, we assess the merits of using linear sweep voltammetry for the task and suggest possible alternative strategies. Most generally, whilst noting that equations (5)–(7) are by no means the only approach to amperometric sensing, we seek to generically advocate the benefits of the potential synergy of modelling/simulation in guiding and evaluating the experimental development of electrochemical sensors and to highlight the many interplaying factors which control in a complex way the formulation of an optimum design.

## 2. Theory

In this section, the simulation models employed in this work are presented before the computational methods are introduced.

### 2.1. Simulation Models

As mentioned in the previous section, the amperometric sensing mechanism represented by equations (5)–(7) is studied in this work for a spherical electrode with radius  $r_e$  based on three different simulation models: first, the system with the deactivated "titrant"  $A$  present in bulk solution under a linear sweep potential waveform, second, the system with the deactivated titrant  $A$  adsorbed irreversibly to the electrode surface under a linear sweep potential waveform, and, third, the system with the deactivated titrant  $A$  adsorbed irreversibly to the electrode surface under a semi-circular sweep potential waveform. Voltammograms are simulated using these three models before comparing between them. The choice of a

spherical geometry electrode allows the easy investigation of the transition between macro- and micro-electrodes simply by altering the electrode radius.

The electrode kinetics are described using the Butler-Volmer theory specifying that, for an electrochemical reaction  $A + e^- \rightleftharpoons B$  [Eq. (8)]:

$$j = k_0 \exp \left[ \frac{-\alpha F(E - E_f^0)}{RT} \right] c_{A_0} - k_0 \exp \left[ \frac{(1 - \alpha) F(E - E_f^0)}{RT} \right] c_{B_0} \quad (8)$$

where  $j$  is the flux of the reductant on the electrode surface,  $k_0$  is the standard rate constant for this electrochemical reaction,  $c_{A_0}$  and  $c_{B_0}$  are the concentrations of species  $A$  and  $B$  at the electrode surface respectively,  $\alpha$  is the transfer coefficient,  $F$  is the Faraday constant,  $R$  is the ideal gas constant,  $T$  is the temperature,  $E$  is the electrode potential, and  $E_f^0$  is the formal potential of the  $A/B$  redox couple.

In the following sections, the three types of simulation models are described in detail, namely the 'solution titrant' model, the 'adsorbed titrant' model with a linear sweep potential waveform, and the 'adsorbed titrant' model with a semi-circular sweep potential waveform.

### 2.1.1. The 'Solution Titrant' Model

The first model is represented by equations (5)–(7) with all species in the solution phase and the electron transfer taking place at a hemi-spherical electrode. The relative fast homogeneous kinetics, described in equation (6), resemble a "titration" reaction for the species  $X$  in the vicinity of the electrode. This leads first to the formation of species  $C$  and then its detection at more negative potentials as a result of the second electrode process given in equation (7). The potential waveform is formulated by two linear sweep potential waveforms in opposing directions leading to a potential  $E(t)$  at time  $t$  [Eq. (9)]:

$$E(t) = \begin{cases} E_{t=0} - \nu t; & \text{for } 0 < t \leq \frac{t_{\text{sim}}}{2} \\ E_{\text{switch}} + \nu(t - \frac{t_{\text{sim}}}{2}); & \text{for } \frac{t_{\text{sim}}}{2} < t < t_{\text{sim}} \end{cases} \quad (9)$$

where  $E_{t=0}$  is the initial potential of the sweep, and  $\nu$  is the scan rate of the linear sweep. At time  $t = \frac{t_{\text{sim}}}{2}$ , the potential reaches  $E_{\text{switch}}$  and the potential sweep changes direction.

The diffusion equation of the species  $j$  under spherical coordinates is, according to Fick's second law [Eq. (10)]:

$$\frac{\partial c_j}{\partial t} = D \nabla^2 c_j = D \left( \frac{\partial^2 c_j}{\partial r^2} + \frac{2}{r} \frac{\partial c_j}{\partial r} \right) \quad (10)$$

Which, combined with the chemical reaction (6), leads to the full set of diffusion equations for this system [Eq. (11)]:

$$\begin{cases} \frac{\partial c_A}{\partial t} = D_A \left( \frac{\partial^2 c_A}{\partial r^2} + \frac{2}{r} \frac{\partial c_A}{\partial r} \right) \\ \frac{\partial c_B}{\partial t} = D_B \left( \frac{\partial^2 c_B}{\partial r^2} + \frac{2}{r} \frac{\partial c_B}{\partial r} \right) - k_C^{\text{Homo}} c_B c_X \\ \frac{\partial c_X}{\partial t} = D_X \left( \frac{\partial^2 c_X}{\partial r^2} + \frac{2}{r} \frac{\partial c_X}{\partial r} \right) - k_C^{\text{Homo}} c_B c_X \\ \frac{\partial c_C}{\partial t} = D_C \left( \frac{\partial^2 c_C}{\partial r^2} + \frac{2}{r} \frac{\partial c_C}{\partial r} \right) + k_C^{\text{Homo}} c_B c_X \\ \frac{\partial c_P}{\partial t} = D_P \left( \frac{\partial^2 c_P}{\partial r^2} + \frac{2}{r} \frac{\partial c_P}{\partial r} \right) \\ D_A = D_B = D_X = D_C = D_P \end{cases} \quad (11)$$

where  $k_C^{\text{Homo}}$  is the homogeneous chemical rate constant such that the chemical reaction rate is equal to  $k_C^{\text{Homo}} c_B c_X$ . All species are assumed to have the same diffusion coefficient.

The boundary conditions set for all species' concentrations at the beginning of the simulations are set in the same way they are set at the edge of the simulation space remote from the electrode surface throughout the simulation period [Eq. (12)]:

$$t = 0, r_e \leq r \leq r_{\text{max}}; t > 0, r = r_{\text{max}} \begin{cases} c_A = c_A^* \\ c_B = 0 \\ c_X = c_X^* \\ c_C = 0 \\ c_P = 0 \end{cases} \quad (12)$$

where  $c_A^*$  and  $c_X^*$  are the bulk concentrations of species  $A$  and  $X$  respectively, and the outer space  $r_{\text{max}}$  of the simulation is defined as  $r_{\text{max}} = r_e + \sqrt{6D t_{\text{sim}}}$  which means the simulation space is set to be much higher than the distance from the electrode for the concentration perturbation to occur, being around:  $\sqrt{\langle (r - r_e)^2 \rangle} = \sqrt{2D t_{\text{sim}}}$  due to Brownian motion<sup>[35,36]</sup>, to make sure the simulation process is independent of the far edge boundary  $r_{\text{max}}$ .

At the electrode surface, the electroactive species  $A$ ,  $B$ ,  $C$  and  $P$  are set according to the Butler-Volmer theory while a no-flux boundary is set for species  $X$  since it is electro-inactive [Eq. (13)]:

$$\left\{ \begin{array}{l} D_A \left( \frac{\partial c_A(r,t)}{\partial r} \right)_{r=r_e} = k_0 \exp \left[ \frac{-\alpha F (E - E_{f,A/B}^0)}{RT} \right] c_A(r_e, t) \\ - k_0 \exp \left[ \frac{(1-\alpha) F (E - E_{f,A/B}^0)}{RT} \right] c_B(r_e, t) \\ D_B \left( \frac{\partial c_B(r,t)}{\partial r} \right)_{r=r_e} = -D_A \left( \frac{\partial c_A(r,t)}{\partial r} \right)_{r=r_e} \\ \left( \frac{\partial c_X(r,t)}{\partial r} \right)_{r=r_e} = 0 \\ D_C \left( \frac{\partial c_C(r,t)}{\partial r} \right)_{r=r_e} = k'_0 \exp \left[ \frac{-\alpha F (E - E_{f,C/P}^0)}{RT} \right] c_C(r_e, t) \\ - k'_0 \exp \left[ \frac{(1-\alpha) F (E - E_{f,C/P}^0)}{RT} \right] c_P(r_e, t) \\ D_P \left( \frac{\partial c_P(r,t)}{\partial r} \right)_{r=r_e} = -D_C \left( \frac{\partial c_C(r,t)}{\partial r} \right)_{r=r_e} \end{array} \right. \quad (13)$$

$$\left\{ \begin{array}{l} T = 0, 1 \leq R \leq R_{\max}; T > 0, R = R_{\max} \\ \left. \begin{array}{l} C_A = 1 \\ C_B = 0 \\ C_X = \frac{C_X^*}{C_A^*} \\ C_C = 0 \\ C_P = 0 \end{array} \right\} \quad (15)$$

$$\left\{ \begin{array}{l} \left( \frac{\partial c_A(R,T)}{\partial R} \right)_{R=1} = K_0 e^{-\alpha \theta} C_A(1, T) - K_0 e^{(1-\alpha)\theta} C_B(1, T) \\ d_B \left( \frac{\partial c_B(R,T)}{\partial R} \right)_{R=1} = - \left( \frac{\partial c_A(R,T)}{\partial R} \right)_{R=1} \\ \left( \frac{\partial c_X(R,T)}{\partial R} \right)_{R=1} = 0 \\ d_C \left( \frac{\partial c_C(R,T)}{\partial R} \right)_{R=1} = K'_0 e^{-\alpha \left( \theta - \theta_{f,C/P} \right)} C_C(1, T) \\ - K'_0 e^{(1-\alpha)(\theta - \theta_{f,C/P})} C_C(1, T) \\ d_P \left( \frac{\partial c_P(R,T)}{\partial R} \right)_{R=1} = -d_C \left( \frac{\partial c_C(R,T)}{\partial R} \right)_{R=1} \end{array} \right. \quad (16)$$

To present the simulation results in a simple and universal manner, dimensionless parameters are employed in this work as shown in Table 1.

Therefore, we can convert the Equations (11)–(13) to their dimensionless counterparts [Eqs. (14)–(17)]:

$$\left\{ \begin{array}{l} \frac{\partial C_A}{\partial T} = d_A \left( \frac{\partial^2 C_A}{\partial R^2} + \frac{2}{R} \frac{\partial C_A}{\partial R} \right) \\ \frac{\partial C_B}{\partial T} = d_B \left( \frac{\partial^2 C_B}{\partial R^2} + \frac{2}{R} \frac{\partial C_B}{\partial R} \right) - K_C^{\text{Homo}} C_B C_X \\ \frac{\partial C_X}{\partial T} = d_X \left( \frac{\partial^2 C_X}{\partial R^2} + \frac{2}{R} \frac{\partial C_X}{\partial R} \right) - K_C^{\text{Homo}} C_B C_X \\ \frac{\partial C_C}{\partial T} = d_C \left( \frac{\partial^2 C_C}{\partial R^2} + \frac{2}{R} \frac{\partial C_C}{\partial R} \right) + K_C^{\text{Homo}} C_B C_X \\ \frac{\partial C_P}{\partial T} = d_P \left( \frac{\partial^2 C_P}{\partial R^2} + \frac{2}{R} \frac{\partial C_P}{\partial R} \right) \\ d_A = d_B = d_X = d_C = d_P \end{array} \right. \quad (14)$$

where  $\theta_{f,C/P} = \frac{F}{RT} (E_{f,C/P}^0 - E_{f,A/B}^0)$ .

$$\theta(T) = \begin{cases} \theta_{T=0} - \sigma T & \text{for } 0 \leq T < T_{\max}/2 \\ \theta_{T=0} + \sigma(T - T_{\max}) & \text{for } T_{\max}/2 \leq T \leq T_{\max} \end{cases} \quad (17)$$

The next section introduces the second simulation model where the titrant is adsorbed on the electrode surface.

### 2.1.2. The 'Adsorbed Titrant' Model with a Linear Sweep

In the second model, we set the species A and B adsorbed on the electrode surface leaving everything else the same as in the previous section. Adsorbed and aqueous species are treated fundamentally differently in this model. Species X, C, P are in the solution phase and treated as having concentrations at discretised space points extending out into solution, an outer boundary point which is not influenced by the electrode activities, hence with a constant concentration, throughout the simulation, and also a concentration at the inner boundary point which is at the electrode surface. Species A and B are irreversibly adsorbed to the surface. Thus, they only have concentrations at the inner boundary space point. Therefore, two new parameters – the surface concentrations  $\Gamma_A$  and  $\Gamma_B$  ( $\text{mol m}^{-2}$ ) – are introduced to describe the concentrations for the adsorbed species A and B, respectively.

A series of changes are made to obtain the dimensionless equations for this model. First, the reference concentration is switched to  $C_X^*$  due to the species A no longer existing in solution. Second, the dimensionless forms of the surface

**Table 1.** Transformation of dimensional parameters to dimensionless parameters for the 'solution titrant' model. Note the subtle difference between the symbol for temperature ( $T$ ) dimensionless time ( $T$ ).

Dimensionless Parameter	Conversion
Concentration of species j	$C_j = \frac{c_j}{C_X^*}$
Diffusion coefficient of species j	$d_j = \frac{D_j}{D_A}$
Radial distance	$R = \frac{r}{r_e}$
Scan rate	$\sigma = \frac{v}{D_A} \frac{F}{RT}$
Time	$T = \frac{t}{D_A} \frac{F}{RT}$
Potential	$\theta = \frac{F}{RT} (E - E_{f,A/B}^0)$
Electrochemical Rate Constant	$K_0 = \frac{k_0 \Gamma_A}{D_A}$
Chemical Rate Constant	$K_C^{\text{Homo}} = \frac{k_C^{\text{Homo}} C_A^* \Gamma_A^2}{D_A}$
Current	$J = \frac{i}{2\pi F r_e D_A C_A^*}$

concentrations for adsorbed species *A* and *B* at the electrode surface have become surface coverages, which can be related to the maximum surface concentration:  $\xi_i = \frac{\Gamma_i}{\Gamma_{\max}}$ . Further, these two reference parameters are related by a single dimensionless independent parameter  $B_X = \frac{r_e c_X^*}{\Gamma_{\max}}$ . Third, as the electrochemical reaction happens entirely adsorbed on the surface, the dimensionless electrochemical rate constant has a different  $r_e$  dependence than in the previous model. Therefore, the rate constants for the two electrochemical reactions become Equation (18):

$$\begin{cases} K_0 = \frac{k_0 r_e^2}{D_X} \\ K'_0 = \frac{k'_0 r_e}{D_X} \end{cases} \quad (18)$$

Finally, the calculation for the chemical rate constant ( $K_C^{\text{Het}}$ ) also differs from the previous model ( $K_C^{\text{Homo}}$ ) as the chemical reaction now only occurs at the surface of the electrode. The detailed conversions between the dimensional and the dimensionless parameters are shown in Table 2.

The diffusion equations needed to be solved are only for the aqueous species *X*, *C*, and *P* which all follow Equation (10), since there is no chemical reaction in the solution phase. Thus, the dimensionless diffusion equation for these three species are given in Equation (19):

$$\frac{\partial C_j}{\partial T} = D \nabla^2 C_j = d_j \left( \frac{\partial^2 C_j}{\partial R^2} + \frac{2}{R} \frac{\partial C_j}{\partial R} \right) \quad (19)$$

The dimensionless boundary conditions are given in Equations (20)–(22):

$$T = 0, \quad 1 \leq R \leq R_{\max}; \quad T > 0, \quad R = R_{\max} \begin{cases} C_X = 1 \\ C_C = 0 \\ C_P = 0 \end{cases} \quad (20)$$

$$T = 0 \begin{cases} \xi_A = \xi_A^* \\ \xi_B = 0 \end{cases} \quad (21)$$

**Table 2.** Transformation of dimensional parameters to dimensionless parameters for the 'adsorbed titrant' model with a linear sweep or a semi-circular sweep potential waveform. Note the subtle difference between the symbol for temperature (*T*) and dimensionless time (*T*).

Dimensionless Parameter	Conversion
Concentration of species <i>j</i>	$C_j = \frac{c_j}{c_i^*}$
Surface coverage of species <i>j</i>	$\xi_i = \frac{\Gamma_i}{\Gamma_{\max}}$
Diffusion coefficient of species <i>j</i>	$d_j = \frac{D_j}{D_X^*}$
Concentration constant	$B_X = \frac{r_e c_X^*}{\Gamma_{\max}}$
Radial distance	$R = \frac{r}{r_{\max}}$
Scan rate	$\sigma = \frac{r_e^2}{D_X^*} \frac{F}{RT} \nu$
Time	$T = \frac{D_X^* t}{r_e^2}$
Potential	$\theta = \frac{F}{RT} (E - E_{f,A/B}^0)$
Electrochemical Rate Constant <i>A/B</i>	$K_0 = \frac{k_0 r_e^2}{D_X^*}$
Chemical Rate Constant	$K_C^{\text{Het}} = \frac{k'_c \Gamma_{\max} r_e}{D_X}$
Electrochemical Rate Constant <i>C/P</i>	$K'_0 = \frac{k'_0 r_e}{D_X}$
Current	$j = \frac{2\pi F r_e D_X c_X^*}{\Gamma_{\max}}$

$$\begin{cases} \frac{\partial \xi_A(T)}{\partial T} = -K_0 e^{-\alpha \theta} \xi_A + K_0 e^{(1-\alpha)\theta} \xi_B \\ \frac{\partial \xi_B(T)}{\partial T} = -\frac{\partial \xi_A(T)}{\partial T} - K_C^{\text{Het}} B_X C_X(1, T) \xi_B \\ d_X \left( \frac{\partial C_X(R, T)}{\partial R} \right)_{R=1} = K_C^{\text{Het}} C_X(1, T) \xi_B \\ d_C \left( \frac{\partial C_C(R, T)}{\partial R} \right)_{R=1} = K'_0 e^{-\alpha \left( \theta - \theta_{f, (C/P)} \left( \frac{\xi}{\xi} \right) \right)} C_C(1, T) \\ - K'_0 e^{(1-\alpha) \left( \theta - \theta_{f, (C/P)} \left( \frac{\xi}{\xi} \right) \right)} C_P(1, T) \\ - K_C^{\text{Het}} C_X(1, T) \xi_B \\ d_P \left( \frac{\partial C_P(R, T)}{\partial R} \right)_{R=1} = -K'_0 e^{-\alpha \left( \theta - \theta_{f, (C/P)} \left( \frac{\xi}{\xi} \right) \right)} C_C(1, T) \\ + K'_0 e^{(1-\alpha) \left( \theta - \theta_{f, (C/P)} \left( \frac{\xi}{\xi} \right) \right)} C_P(1, T) \end{cases} \quad (22)$$

where it is worth noting that the boundary condition at the electrode surface for aqueous species is based on  $d_i \left( \frac{\partial C_i(R, T)}{\partial R} \right)_{R=1}$  and determining this value is necessary for determining the transport of material to and from the electrode surface. As transport to and from the electrode surface is impossible for the adsorbed species, the inner boundary condition is instead based on  $\frac{\partial \xi_i(T)}{\partial T}$  and the conversion between these time- and space-differentials is dependent on  $B_X$ .

### 2.1.3. The 'Adsorbed Titrant' Model with a Semi-Circular Sweep

As for the third model, the only difference in the simulation in comparison with the second model is that this model employs a semi-circular sweep in the practice of the voltammetry.

The dimensionless semi-circular potential wave used in this paper is described by Equation (23) below and a schematic of which is shown in Figure 1.

$$\theta(T) = \pm \sqrt{A^2 - [\sigma_{\text{avg}}(T - cT_{\max})]^2} + \theta_{\text{shift}} \quad (23)$$

where  $\theta_{\text{shift}}$  is the theta value at which the two quarter-circles meet and the scan rate becomes instantaneously and theoretically infinite; *A* is the amplitude and denotes the difference in  $\theta$  between the starting  $\theta$  value and the  $\theta_{\text{shift}}$  or the radius of the waveform's quarter-circles ( $2A$  equals the total potential range);  $\sigma_{\text{avg}}$  is dimensionless average scan rate; *T* is again the dimensionless time; *c* equals the *T*-value of the midpoint of the current quarter-circle divided by  $T_{\max}$  which is the total time of the voltammetric sweep (*c* is 0 for the first quarter-circle when  $\theta(T) > c$  is 1 for the second quarter-circle when  $\theta(T) < \theta_{\text{shift}}$ ).

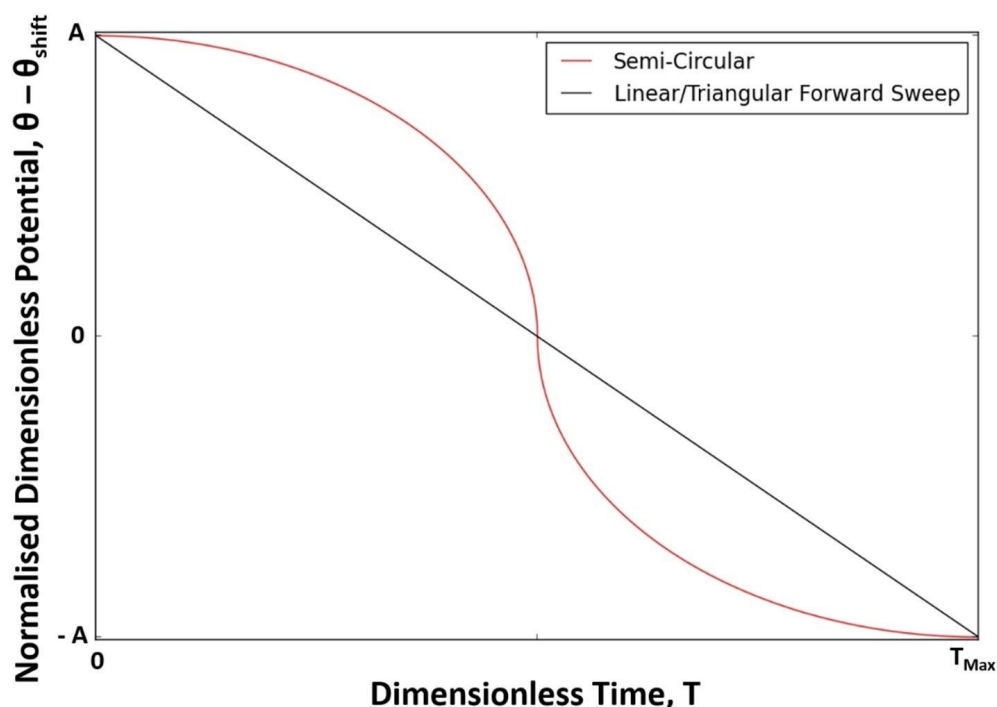


Figure 1. Illustrations of a semi-circular waveform and a linear sweep waveform with equal average scan rate of  $\alpha_{avg}$ .

## 2.2. Computational Methods

The simulations were performed using home written C++ programs with *OpenMP* for parallel computing. The diffusion equations were solved using the finite difference method by discretising the dimensionless diffusion equation into an expanding space grid<sup>[37]</sup> and using the backward implicit method.<sup>[25]</sup> To solve the multi-diagonal sparse matrix given by the implicit method, the root-finding Newton-Raphson method was applied. Note that the Newton-Raphson method was iterated until the average error was smaller than  $10^{-9}$ . The resulting voltammograms were verified by ensuring the error of mass conservation was below  $10^{-10}\%$  and thorough testing<sup>[38]</sup> was performed using convergence testing, and comparison with theoretical peak currents. A thorough account of the testing and validation for the models is shown in the Supplementary Information. The plotting was carried out in *Python* with the packages *NumPy*, *SciPy* and *matplotlib* and the tables were plotted in *Origin Pro 2017*.

## 3. Results and Discussion

In this section, simulated results for different designs of amperometric sensors based on mediated electron transfer are presented. These designs include utilisation of a linear sweep potential waveform with the deactivated titrant A in solution, a linear sweep potential waveform with the deactivated titrant A adsorbed irreversibly to the electrode surface, and a semi-circular sweep potential waveform with the deactivated titrant A adsorbed irreversibly to the electrode surface. Corresponding

analysis and discussion are provided and focus on the comparison of these designs and their optimisation for sensing for both macro- and micro- hemispherical electrodes.

### 3.1. Employing the Titrant as a Soluble Additive to the Sample versus Adsorbed onto the Electrode Surface: A Comparison

In this section we consider the voltammetric features we expect to see for the “adsorbed titrant” and “solution titrant” models, how these features change with analyte concentration and the chemical rate constant, and then we compare which of these two approaches to the design of a mediated electron transfer sensor shows best sensitivity and limits of detection.

Simulations were performed first for the design using linear sweep voltammetry and an adsorbed titrant. Presented in Figure 2 are voltammograms for this sensor design with varying concentrations of the analyte species X. The simulation was run with: an electrode radius of 1 mm, a heterogeneous chemical rate constant  $k_c^{het}$  of  $10^6 \text{ M}^{-1} \cdot \text{s}^{-1}$ , a scan rate of  $2 \text{ V} \cdot \text{s}^{-1}$ , a  $k_0$  of  $10^6 \text{ s}^{-1}$ ,  $\alpha$  values of 0.5, an initial surface concentration of  $10^{-6} \text{ mol} \cdot \text{m}^{-2}$  of A, diffusion coefficients of  $10^{-9} \text{ m}^2 \cdot \text{s}^{-1}$  for the species in solution, a difference in formal potentials of the electrochemical couples of 257 mV, and a  $k'_0$  of  $10 \text{ cm} \cdot \text{s}^{-1}$ . The values of  $k_0$  and  $k'_0$  are chosen such that both electrochemical couples are in the Nernstian (fully electrochemically reversible) limit due to the fast electrode kinetics. The electrode radius, scan rate and initial surface concentration are chosen as they would be experimentally realistic for a sensor design, while the heterogeneous chemical rate constant,  $\alpha$  values, diffusion



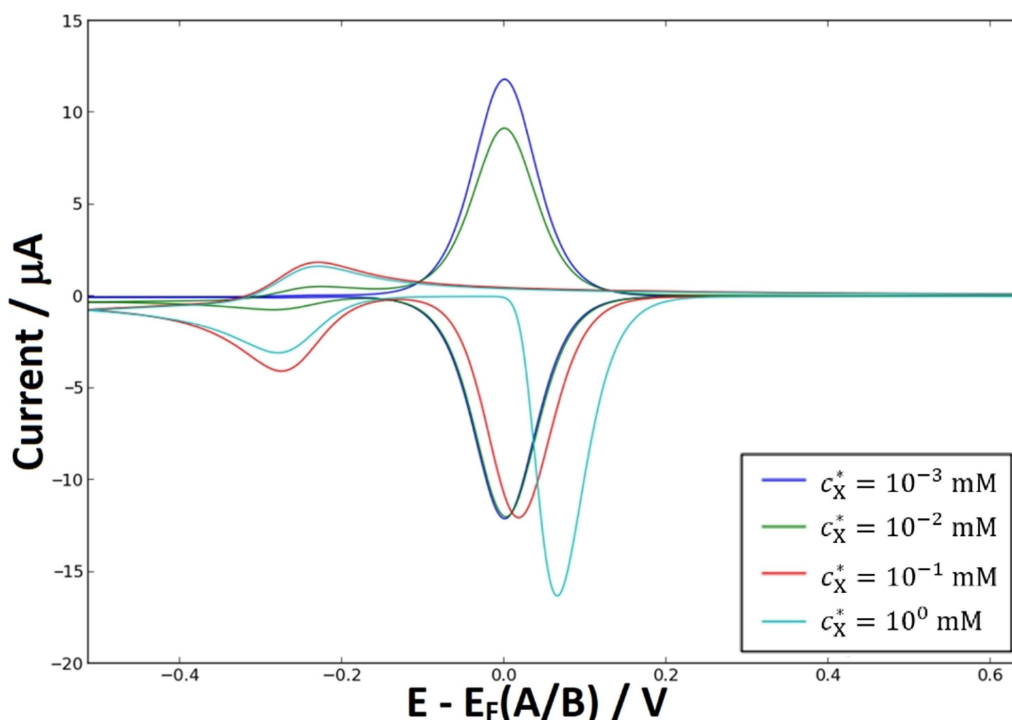


**Figure 2.** Voltammograms highlighting the voltammetric features expected for a sensor utilising linear sweep potential waveforms and titrant species adsorbed to the electrode surface as well as how these features are affected by different analyte concentrations between  $10^{-3}$  mM and 1 mM as specified in the figure legend. In this example, the simulation was run with: an electrode radius of 1 mm, a heterogeneous chemical rate constant  $k_c^{\text{het}}$  of  $10^6 \text{ M}^{-1}\text{s}^{-1}$ , a scan rate of  $2 \text{ V}\cdot\text{s}^{-1}$ , a  $k_0$  of  $10^6 \text{ s}^{-1}$ ,  $\alpha$  values of 0.5, an initial surface concentration of  $10^{-6} \text{ mol}\cdot\text{m}^{-2}$  of A, diffusion coefficients of  $10^{-9} \text{ m}^2\cdot\text{s}^{-1}$  for the species in solution, a difference in formal potentials of the electrochemical couples of 257 mV, and a  $k'_0$  of  $10 \text{ cm}\cdot\text{s}^{-1}$ .

coefficients and difference in formal potentials of the electrochemical couples are similarly chosen as they are also feasible for a chemical system with which a mediated electron transfer sensor might be coupled. In particular, the surface concentration matches the typical value for an organic monolayer, the  $\alpha$  value of many electron transfers deviate little from 0.5, and the diffusion coefficients of aqueous species has the same order of magnitude as  $10^{-9} \text{ m}^2\cdot\text{s}^{-1}$ .<sup>[22]</sup>

It can be seen that there are a variety of features which are dependent on the analyte concentration which, of course, controls the rate of the chemical step. Firstly, we consider the case of a low analyte concentration of  $c_X^* = 10^{-3} \text{ mM}$  for which the chemical reaction rate is thus sufficiently slow that negligible analytical reagent C is produced, and the A/B couple is negligibly perturbed. Only one wave is present, and it is related to the adsorbed A/B couple. It is symmetric with respect to both  $E_{f,A/B}^0$  and the potential-axis as diffusion does not occur either towards or away from the electrode surface; the same finite charge is transferred to the adsorbed monolayer during both the forward and backward scans. Under Nernstian conditions for the A/B couple, the current can be calculated as Equation (24):

$$\frac{I}{FA} = \frac{\Gamma_t F v e^{\theta}}{RT(e^{\theta} + 1)^2} \quad (24)$$

and the peak current as Equation (25):

$$\frac{I_{\text{peak}}}{FA} = \frac{Fv\Gamma_t}{4RT} \quad (25)$$

where  $\Gamma_t$  equals the initial surface concentration of A (in this case corresponding to  $10^{-6} \text{ mol}\cdot\text{m}^{-2}$ , typical for an organic monolayer);  $\theta$  is equal to  $\frac{F}{RT}(E - E_{f,A/B}^0)$ ;  $F$  is the Faraday constant;  $R$  is the gas constant;  $T$  is the temperature, assumed to be 298 K in this case;  $E$  is the potential;  $E_{f,A/B}^0$  is the formal potential of the A/B couple; and  $v$  is the scan rate.

If the analyte concentration is increased, a number of effects are seen. Firstly, the backward peak of the A/B couple is reduced as the activated titrant B species is removed by the heterogeneous chemical reaction with the analyte X species to form electroactive analytical reagent C species. Secondly, a second wave becomes visible at more negative potentials. This possesses the shape of a typical voltammogram seen for an electroactive solution species undergoing electron transfer at a macro-electrode and is caused by the C/P couple. We denote this wave to be the analytical C/P wave. The size of its peak is dependent on the analyte concentration and this will be used by a sensor to indirectly determine the analyte concentration.

At high analyte concentrations, such as  $c_X^* = 0.1$  or 1 mM, the forward A/B couple peak becomes significantly perturbed. The peak shifts to higher potentials, and greater asymmetry is introduced to the wave's character. The current induced by the A/B couple during the backward scan has disappeared as no B is left on the electrode surface at this point in time. The

waveshape of the  $A/B$  couple begins to increasingly resemble that for an irreversible reduction and the  $A/B$  peak current increases as the analyte concentration is increased. It can be seen that at high analyte concentrations, increasing  $c_X^*$  further actually results in the peak current of the analytical  $C/P$  wave decreasing. This possibly unexpected effect of an excessively fast chemical step reducing the analytical peak current is of important consideration and discussed more in our multivariate analysis below.

Figure 3 shows the corresponding voltammograms for the design utilising a linear sweep potential waveform and the deactivated titrant species  $A$  in bulk solution rather than adsorbed to the electrode surface, and how its corresponding features vary with the concentration of analyte  $X$ . The simulation was run with: an electrode radius of  $1\text{ mm}$ , a homogeneous chemical rate constant  $k_c^{\text{homo}}$  of  $10^6\text{ M}^{-1}\text{ s}^{-1}$ , a scan rate of  $2\text{ V s}^{-1}$ , a  $k_0$  of  $10\text{ cm s}^{-1}$ ,  $\alpha$  values of  $0.5$ , a bulk concentration of  $1\text{ mM}$  of  $A$ , diffusion coefficients of  $10^{-9}\text{ m}^2\text{ s}^{-1}$  for the species in solution, a difference in formal potentials of the electrochemical couples of  $257\text{ mV}$ , and a  $k'_0$  of  $10\text{ cm s}^{-1}$ . Where possible, parameters have been chosen to match those used in the above simulation with adsorbed titrant. The homogeneous chemical reaction rate has the same units as the heterogeneous chemical rate constant and so has been given the same value, assuming the rate is equally fast for a reaction between both species in solution as for a reaction between adsorbed  $B$  and  $X$  in solution. The  $k_0$  value was chosen to be  $10\text{ cm s}^{-1}$  so that the electrode kinetics remain sufficiently fast

such that Nernstian behaviour is maintained. An initial bulk concentration of deactivated titrant  $A$  of  $1\text{ mM}$  is chosen, as it is the largest concentration we might expect to be used in a sensor design before limitations of solubility arise.

Figure 3 displays qualitatively similar features as those displayed in Figure 2. At a low analyte concentration, such as  $c_X^* = 10^{-3}\text{ mM}$ , only one peak is observed and associated with an unperturbed  $A/B$  couple. In this case, the waveshape is typical of a reversible reduction of a solution species, rather than of an adsorbed species, and possesses a diffusional tail at high over-potentials as  $A$  material continues to diffuse to the electrode from bulk solution. As the analyte concentration increases, the  $A/B$  back-peak decreases and disappears, a peak at more negative potentials induced by the  $C/P$  couple appears, and, at high analyte concentrations, the forward  $A/B$  peak shifts to more positive potentials and increasingly resembles a chemically irreversible waveshape.

We next compare results from both models, using the conditions presented as benchmarks for what might be used in such a sensor design, since a true exact equivalence in the conditions cannot be drawn between the two models. Thus, we compare what would be feasible for both designs.

We see that the “solution titrant” design gives greater currents than the “adsorbed titrant” design at all points in the voltammogram by approximately an order of magnitude. This is not unexpected as the amount of  $A$  material available for reduction is limited to a monolayer-thick shell around the electrode for the “adsorbed titrant” design and this material is

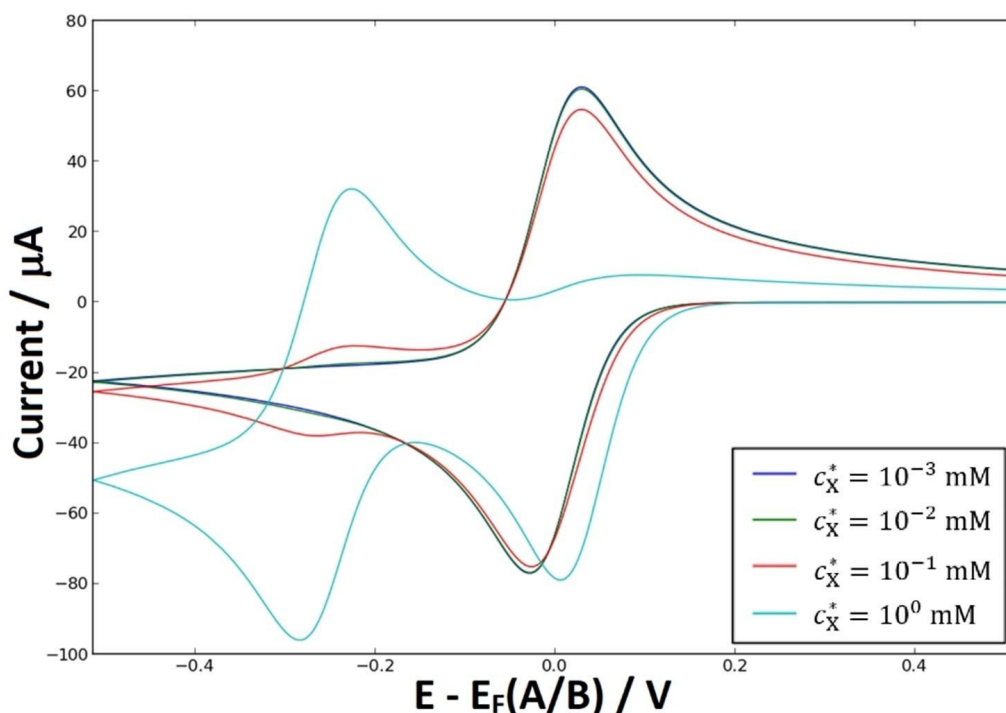


**Figure 3.** Voltammograms highlighting the voltammetric features expected for a sensor utilising linear sweep potential waveforms and titrant species adsorbed to the electrode surface as well as how these features are affected by different analyte concentrations. In this example the simulation was run with: an electrode radius of  $1\text{ mm}$ , a homogeneous chemical rate constant  $k_c^{\text{homo}}$  of  $10^6\text{ M}^{-1}\text{ s}^{-1}$ , a scan rate of  $2\text{ V s}^{-1}$ , a  $k_0$  of  $10\text{ cm s}^{-1}$ ,  $\alpha$  values of  $0.5$ , a bulk concentration of  $1\text{ mM}$  of  $A$ , diffusion coefficients of  $10^{-9}\text{ m}^2\text{ s}^{-1}$  for the species in solution, a difference in formal potentials of the electrochemical couples of  $257\text{ mV}$ , and a  $k'_0$  of  $10\text{ cm s}^{-1}$ .



not replenished by diffusion from a bulk solution, unlike for the “solution titrant” design. Thus, less material is reduced over the course of a forward scan for the “adsorbed titrant” design. This remains true even under the fast  $2\text{ V}\cdot\text{s}^{-1}$  scan rate used in the presented simulations, which limits the thickness of the diffusion layer of A.

Relatedly, with less A material reduced, less B material is available for chemical reaction, and thus less total C material is generated. However, the “adsorbed titrant” design restricts the chemical reaction to occur only at the electrode surface, unlike the “solution titrant” design which allows B material to diffuse from the surface and thus react to form C at a distance from the electrode, reducing the amount of C material produced that is available for the subsequent electron transfer. Hence, though there is still a difference of an order of magnitude between the C/P peak currents (relative to background current) produced by the two models, this difference is not as large as that observed for the A/B peak currents. Alongside the larger C/P induced current, we observe a greater sensitivity to the analyte concentration *at analyte concentrations sufficiently large to produce a distinguishable C/P peak*.

An important difference between the voltammograms produced by the two designs is that the A/B diffusional tail is only present for the “solution titrant” design. The combination of the diffusional tail obscuring the C/P peak and the greater C/P peak current sensitivity causing the peak current to reduce significantly as analyte concentration is reduced results in the C/P peak becoming indistinguishable at higher analyte concentrations relative to the “adsorbed titrant” model. This gives a higher limit of detection. This can be observed for  $c_X^* = 10^{-2}\text{ mM}$  in Figure 2 and Figure 3 as the C/P peak is only distinguishable for the “adsorbed titrant” model.

We conclude that the “adsorbed titrant” design is thus preferable to using titrant dissolved in the sample solution for a mediated electron transfer sensor, despite the greater sensitivity and currents achievable with a “solution titrant”, as the limits of detection achievable are lower. Furthermore, from a practical perspective, the “adsorbed titrant” design is preferable, not least since the sensor is ‘reagent free’ in not needing solution phase additives. Further, efforts need not be made to accurately and precisely dilute the deactivated titrant species A before each sensing measurement, thus reducing the time to use the sensor, reducing the required expertise to use the sensor accurately and improving the accuracy of the sensor by removing a factor of human error. Furthermore, producing and storing electrodes with pre-functionalised surfaces is more convenient and space-efficient than producing and storing electrodes and titrant material separately. Hence the “adsorbed titrant” design remains the subject of investigation for the next sections of this paper.

### 3.2. A Multivariate Analysis of the Analytical Current Response for Linear Sweep Voltammetry

To perform a multi-variate analysis for the optimisation of the “adsorbed titrant/linear sweep voltammetry” sensor design, the

parameters  $c_X^*$ ,  $r_e$ ,  $k_c^{\text{Het}}$ , and  $\nu$  were varied and the resulting simulated Faradaic current densities for the analytical C/P voltammetric peak are tabulated in Table 3.  $c_X^*$  was varied between  $1\text{ }\mu\text{M}$  and  $0.1\text{ mM}$ ,  $r_e$  was varied between  $1\text{ }\mu\text{m}$  and  $1\text{ mm}$ ,  $k_c^{\text{Het}}$  was varied between  $10^3\text{ M}^{-1}\cdot\text{s}^{-1}$  and  $10^9\text{ M}^{-1}\cdot\text{s}^{-1}$ , and  $\nu$  was varied between  $2\text{ mV}\cdot\text{s}^{-1}$  and  $2\text{ V}\cdot\text{s}^{-1}$ . These ranges and values are chosen as they encompass the typical ranges of values used experimentally. The analyte concentration coverage is chosen such that the analyte concentration is within the range of concentrations typically studied using electrochemical methods, giving  $0.1\text{ mM}$  as an upper bound, whilst  $1\text{ }\mu\text{M}$  is chosen as it is sufficiently small to reveal the trends concluded from the multivariate analysis while remaining large enough to give sizeable Faradaic analytical peak current densities. The electrode radius range is chosen to include both macro- and micro-electrode regimes including intermediate radius sizes and thus illustrate the effects of transitioning from planar to convergent diffusion regimes. The  $k_c^{\text{Het}}$  range is chosen such that the physical upper limit of  $10^{10}\text{ M}^{-1}\cdot\text{s}^{-1}$  for a bimolecular reaction is not exceeded. The lower limit of the range investigated is chosen because this is the slowest a practical titration reaction will act: as can be seen from Table 3, the results for the analytical current density when  $k_c^{\text{Het}} = 10^3\text{ M}^{-1}\cdot\text{s}^{-1}$  do not generally exceed the values attained by the faster  $k_c^{\text{Het}}$  values investigated, nor do they approach the largest Faradaic analytical current densities seen for a given analyte concentration. The scan rate,  $\nu$ , range investigated encompasses the range that is experimentally practical. Faster scan rates than  $2\text{ V}\cdot\text{s}^{-1}$  tend to have issues with large capacitive currents (as investigated in a later section) and also exceeds the capability of a typical mid-range commercial potentiostat. Slower scan rates than  $2\text{ mV}\cdot\text{s}^{-1}$  not only take longer to run but also introduce issues of natural convection significantly affecting results as the diffusion layer extends far from the electrode surface. The values within these ranges are chosen to follow regular logarithmic intervals, with a compromise exacted between tabular resolution and simulation time.

Values of  $10^6\text{ s}^{-1}$  and  $1\text{ cm}\cdot\text{s}^{-1}$  were chosen for  $k_0$  and  $k'_0$  respectively as these are fast electron transfer rate constants that give results matching Nernstian predictions. Greater irreversibility in  $k'_0$  would be antithetical to optimising a sensor's design as this would only serve to decrease the analytical current. Meanwhile a more irreversible  $k_0$  would shift the A/B peak towards obscuring the C/P peak, restricting the detection limit. Both alpha values are chosen to be 0.5, the difference in the formal potentials of the couples is set to 257 mV (which corresponds to 10 units in dimensionless theta), the diffusion coefficients of all species in solution are  $10^{-9}\text{ m}^2\cdot\text{s}^{-1}$ , and the initial surface concentration of A is  $10^{-6}\text{ mol}\cdot\text{m}^{-2}$ . This surface concentration is chosen as it provides a good estimation of the surface concentration expected from a monolayer of an organic species.

With the purpose of optimising the sensor design, one can investigate the trends evident for each of these parameters on the Faradaic analytical current density, which would be maximised for the analyte concentration of interest in an optimised design. It is useful to consider the current densities

**Table 3.** Tabulation of the peak current densities ( $\mu\text{A cm}^{-2}$ ) of the analytical C/P peak for the system involving a linear sweep voltammetric waveform and the titrant adsorbed to the electrode surface. Four parameters of interest are varied within the limits of physical feasibility: the analyte concentration, the electrode radius, the chemical rate constant and the scan rate. Values of  $10^6 \text{ s}^{-1}$  and  $1 \text{ cm} \cdot \text{s}^{-1}$  were chosen for  $k_0$  and  $k'_0$  respectively, both alpha values are chosen to be 0.5, the formal peak separation is set as 257 mV (which corresponds to 10 units in dimensionless theta), the diffusion coefficients of all species in solution is  $10^{-9} \text{ m}^2 \cdot \text{s}^{-1}$ , and the initial surface concentration of A is  $10^{-6} \text{ mol} \cdot \text{m}^{-2}$ . The entry N/A is given to simulations in which no analytical C/P peak is distinguishable.

[X] [ $\mu\text{M}$ ]	$\log(k_c^{\text{Het}})$ [ $\text{M}^{-1} \cdot \text{s}^{-1}$ ]	$\nu$ [ $\text{mV} \cdot \text{s}^{-1}$ ]	$r_e = 1 \mu\text{m}$	$r_e = 10 \mu\text{m}$	$r_e = 100 \mu\text{m}$	$r_e = 1000 \mu\text{m}$
100	3	2	< 0.01	< 0.01	< 0.01	0.03
		20	0.18	0.21	0.39	0.61
		200	0.79	0.90	1.31	1.48
		2000	0.96	1.24	1.61	1.68
	6	2	< 0.01	< 0.01	< 0.01	0.023
		20	< 0.01	< 0.01	0.11	0.37
		200	0.03	0.36	2.89	4.61
		2000	1.34	18.15	53.70	62.12
	9	2	< 0.01	< 0.01	< 0.01	0.02
		20	< 0.01	< 0.01	0.07	0.30
		200	0.02	0.21	2.09	3.74
		2000	0.65	9.56	35.66	43.05
10	3	2	0.02	0.02	0.03	0.05
		20	0.08	0.08	0.11	0.14
		200	0.10	0.10	0.15	0.16
		2000	0.10	0.13	0.17	0.18
	6	2	< 0.01	< 0.01	< 0.01	0.03
		20	< 0.01	0.01	0.14	0.43
		200	0.04	0.71	4.27	3.77
		2000	24.34	16.50	11.96	11.47
	9	2	< 0.01	< 0.01	< 0.01	0.02
		20	< 0.01	< 0.01	0.08	0.33
		200	0.02	0.28	4.54	3.87
		2000	0.96	19.72	12.72	12.06
1	3	2	< 0.01	< 0.01	< 0.01	0.01
		20	< 0.01	0.01	0.01	0.02
		200	0.01	0.01	0.02	0.02
		2000	N/A	N/A	N/A	N/A
	6	2	< 0.01	< 0.01	< 0.01	0.05
		20	< 0.01	0.03	0.19	0.13
		200	2.32	1.07	0.44	0.38
		2000	4.75	1.72	1.22	1.16
	9	2	< 0.01	< 0.01	< 0.01	0.05
		20	< 0.01	< 0.01	0.20	0.13
		200	0.03	1.22	0.45	0.39
		2000	10.23	1.98	1.28	1.22

rather than the currents as this allows fair comparison of the utility of using differently sized electrodes and easier comparison to expected capacitive currents, which will be investigated later in this paper.

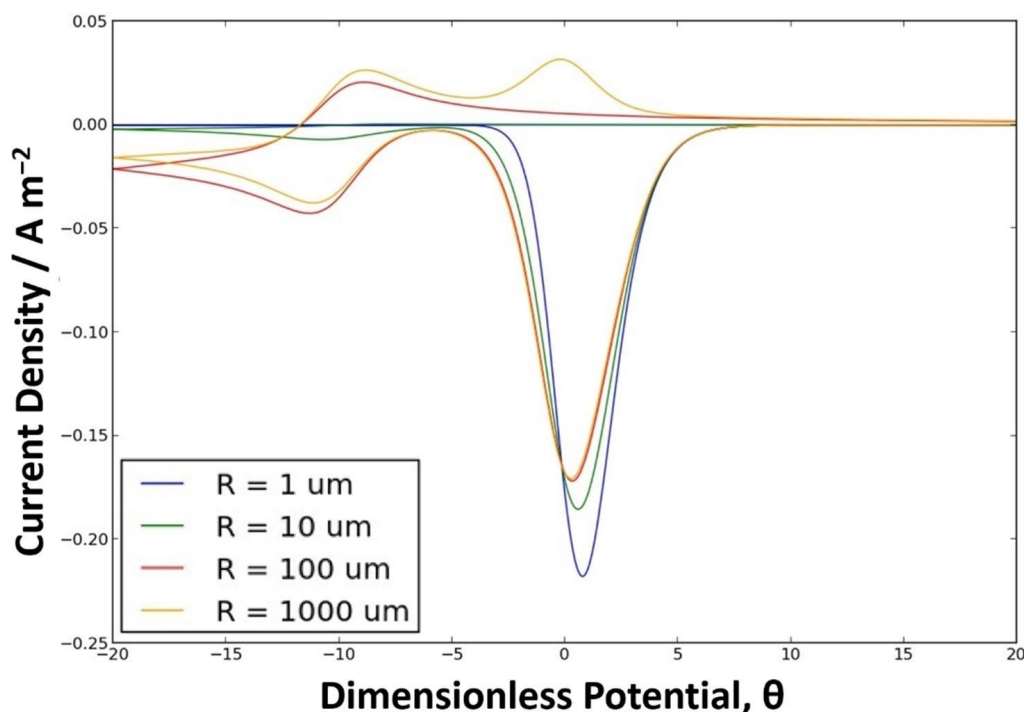
### 3.2.1. Optimising the Electrode Radius

Table 3 illustrates a complex relationship between the Faradaic analytical peak current density and the electrode radius. However, we see that as the concentration of the analyte decreases, the preference of the Faradaic analytical peak current density for a smaller electrode radius increases.

There are a number of examples in Table 3 where varying the electrode radius produces a maximum in the Faradaic analytical peak current density. This provides evidence for at least two competing effects that are dependent on the electrode radius. This maximum is illustrated in Figure 4, which shows the voltammograms for the case of  $k_c^{\text{Het}} = 10^6 \text{ M}^{-1} \cdot \text{s}^{-1}$ ,  $\nu =$

$200 \text{ mV} \cdot \text{s}^{-1}$ , and  $c_x^* = 10 \mu\text{M}$  for varying  $r_e$  between 1 and  $1000 \mu\text{m}$ .

As the electrode radius decreases, the A/B peak shifts to higher potentials and its peak current increases. Greater asymmetry is also introduced into the waveshape. These effects match those reported previously in the literature<sup>[39]</sup> where following kinetics shift the equilibrium at the electrode surface by depleting the electrogenerated product. Initially, this causes an increase in the peak current as the removal of the product prevents its re-oxidation and increases the net flow of electrons; as the impact of the following kinetics on the system increases, the system behaves increasingly irreversibly, with the limiting case being that no re-oxidation can occur due to the product being removed by the following kinetics before it has the opportunity to re-oxidise. By reducing the electrode radius, the impact of the following kinetics on the A/B electrochemical step is increased. This is due to the diffusion regime of the analyte towards the electrode surface shifting from planar to convergent diffusion and thus becoming more efficient: enhancing the replenishing of the analyte at the electrode



**Figure 4.** Voltammograms illustrating the variation in Faradaic current density between designs differing in electrode radius for the case of  $k_c^{\text{Het}} = 10^6 \text{ M}^{-1} \text{ s}^{-1}$ ,  $v = 200 \text{ mV s}^{-1}$ , and  $c_x = 10 \text{ } \mu\text{M}$ .

surface during the reaction and thus the following kinetics' effect on the system.

The impact that the kinetics of the chemical step have on the system underlie the competing, radially dependent effects. If the kinetics are fast, the titrant material is used up before the scan has reached the analytical C/P peak, leaving time for the C species to diffuse away from the electrode surface, as seen for  $r_e = 1 \text{ } \mu\text{m}$  in Figure 4 where the analytical peak is negligible. This effect can even be compounded by the following kinetics shifting the A/B peak to higher potentials and thus extending the time for the C species to diffuse away. If the kinetics are slow, then not all of the B species is converted into C before the analytical C/P peak is complete, as seen for  $r_e = 1000 \text{ } \mu\text{m}$  in Figure 4 where the backward scan produces a peak for the re-oxidation of B.

The diffusion regime also has effects of its own beyond the impact of the chemical step: a more convergent diffusion regime simultaneously allows more efficient diffusion of C away from the electrode surface during the time between the voltammetric peaks but also allows more efficient diffusion of C towards the electrode surface once its reductive wave begins.

The combination of these effects results in an optimal electrode radius for a certain analyte concentration. By reducing the analyte concentration, the impact of the following kinetics is reduced, and so the optimal electrode radius decreases also. Micro-electrodes become increasingly preferable for smaller analyte concentrations, while macro-electrodes are preferable for higher analyte concentrations.

### 3.2.2. Optimising the Reaction Rate Constant

Table 3 similarly portrays a complex relationship between the Faradaic analytical peak current density and the chemical reaction rate constant,  $k_c^{\text{Het}}$ . Examples where varying the value of  $k_c^{\text{Het}}$  produces a maximum in the Faradaic analytical peak current density are present. One of these exemplary cases is illustrated by Figure 5.

The  $k_c^{\text{Het}}$  only affects the kinetics of the chemical step. Similar to how the electrode radius affected the chemical step's impact, increasing  $k_c^{\text{Het}}$  increases the chemical step's impact and, similarly, too great or too weak an impact results in a reduction in the analytical peak current density for the same reasons as described for the electrode radius. The result of this is that, for a given system, there will be an optimal reaction rate constant, and thus a faster titration reaction does not necessarily result in a greater response. What the optimal reaction rate constant for a system will be is dependent on the other 3 parameters investigated. However, the best Faradaic analytical peak current densities are observed for fast chemical rate constants in the range of physical feasibility (i.e. around  $10^6 - 10^9 \text{ M}^{-1} \text{ s}^{-1}$ ).

An explanation is required for the unusual waveshape of the voltammogram in Figure 5 corresponding to  $k_c^{\text{Het}} = 10^9 \text{ M}^{-1} \text{ s}^{-1}$ . The net reduction of A begins at much more positive potentials than expected due to the rapid removal of B by the fast chemical step. However, the analyte concentration at the surface is fully depleted before the titrant material is fully reduced; the chemical reaction becomes dependent on the diffusion of analyte material to the electrode, slowing its rate and producing an inflection in the Faradaic current. The peak

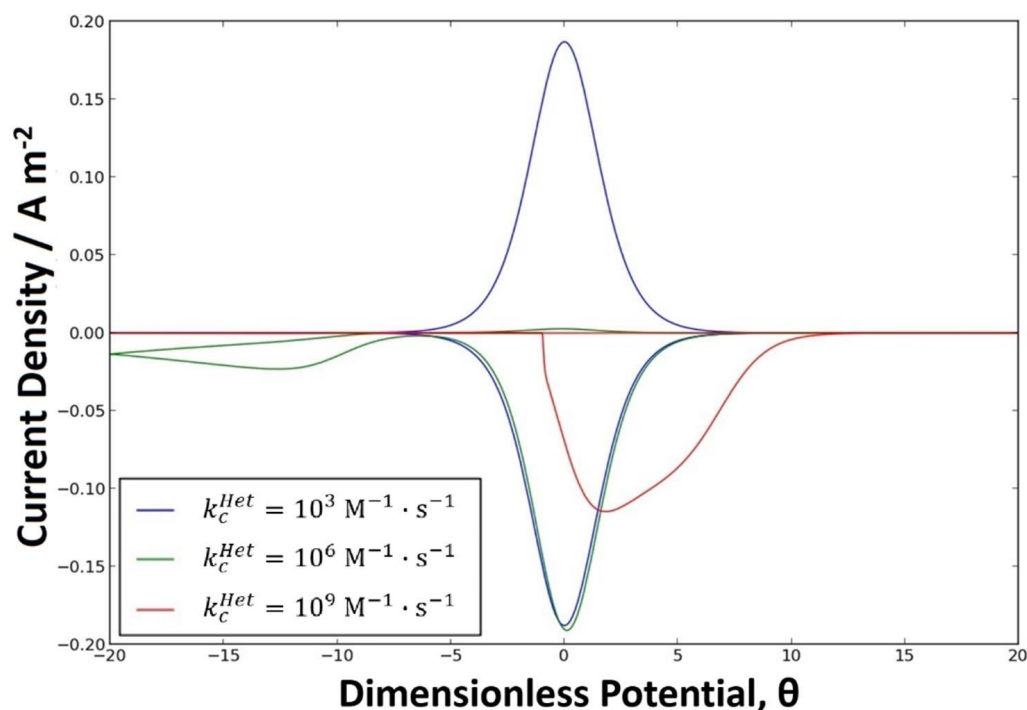


**Figure 5.** Voltammograms illustrating the variation in Faradaic current density between designs differing in the chemical rate constant  $k_c^{Het}$  for the case of  $r_e = 1 \mu\text{m}$ ,  $\nu = 200 \text{ mV}\cdot\text{s}^{-1}$ , and  $c_X^* = 1 \mu\text{M}$ .

occurs when the ratio of A:B is such that the net flow of electrons is maximised. As A begins to run out the current gradually decreases. A sudden drop in current is observed when both A and B are fully depleted by B's reaction with the analyte. This unusual waveshape is only possible in situations where the analyte at the surface depletes before the titrant material is fully reduced *and* all of the titrant material has reacted with the analyte such that the surface concentrations of A and B deplete simultaneously.

### 3.2.3. Optimising the Scan Rate

Within the ranges investigated, according to Table 3, increasing the scan rate always increases the Faradaic analytical peak current density.

The scan rate has a variety of effects on the system. A faster scan rate weakens the impact of the chemical step by providing less time for the chemical reaction to occur. A faster scan rate also introduces greater planar diffusion behaviour around the electrode, as opposed to convergent behaviour, as the diffusion layer is thinner relative to the size of the electrode. A faster scan rate also provides less time for C produced by the chemical step to diffuse away from the electrode surface before it can be reduced. A faster scan rate also results in a larger peak current for the analytical C/P wave (if the diffusion regime has a significant planar contribution) and also a larger peak current for the A/B wave.

Recognising these effects helps to understand the case of  $c_X^* = 1 \mu\text{M}$  and  $k_c^{Het} = 10^3 \text{ M}^{-1}\cdot\text{s}^{-1}$  where, for all  $r_e$  investigated,

increasing the scan rate increases the Faradaic analytical peak current density until, for  $\nu = 2 \text{ V}\cdot\text{s}^{-1}$ , no peak is observed. This is due to the A/B peak's greater dependence on scan rate ( $I_{A/B} \propto \nu^1$  while  $I_{C/P} \propto \nu^{0.5}$  or  $\nu^0$ ) causing the C/P peak to be obscured beneath the current produced by the now-decaying A/B peak.

Table 4 allows insight into the effects of the scan rate beyond the scan rate dependence of the analytical Faradaic peak current density on a macro-electrode, and thus how the scan rate affects the underlying mechanism of the titration. This normalisation is achieved by dividing the analytical current density by  $\sqrt{\nu}$ . By varying  $\nu$  it is evident that there is a maximum in the normalised analytical current density due to the competing demands of minimising the time allowed for the C material to diffuse away from the electrode before the C/P analytical peak and optimising the impact of the chemical step on the A/B couple. Increasing the chemical rate constant shifts the position of this maximum to higher scan rates as the impact of the chemical step is increased, requiring faster scan rates in order to limit its effect. Increasing  $c_X^*$  also shifts the position of this maximum to faster scan rates, with the same reasoning.

### 3.2.4. The Capacitive Current

An important consideration in the design of a sensor is the signal to background ratio. In the case of an electrochemical sensor, it is vital to consider how the Faradaic current compares to the capacitive current, which acts as a background above which the analytical signal needs to be measured.

**Table 4.** Normalised Analytical Current Densities (in  $\mu\text{A}\cdot\text{cm}^{-2}\cdot\text{s}^{0.5}\cdot\text{V}^{-0.5}$ ) extracted for  $r_e = 1\text{ mm}$  from Table 3.

$k_c^{\text{Het}} [\text{M}^{-1}\cdot\text{s}^{-1}]$	$\nu [\text{mV}\cdot\text{s}^{-1}]$	$c_x^* = 1\text{ }\mu\text{M}$	$c_x^* = 10\text{ }\mu\text{M}$	$c_x^* = 100\text{ }\mu\text{M}$
$10^3$	2	0.241	1.169	0.754
	20	0.105	0.955	4.327
	200	0.039	0.364	3.304
	2000	No Peak	0.126	1.188
$10^6$	2	1.008	0.573	0.511
	20	0.897	3.051	2.620
	200	0.855	8.421	10.298
	2000	0.823	8.108	43.927
$10^9$	2	1.016	0.429	0.393
	20	0.902	2.350	2.121
	200	0.868	8.655	8.367
	2000	0.860	8.529	30.444

An electrode will have a certain capacitance, typically in aqueous solution of the order of  $10\text{ }\mu\text{F}\cdot\text{cm}^{-2}$ , which depends on the chemical electrolyte system it is in, for example it will be dependent on the size of the ions that form the double layer, and this is defined as the increase in charge associated with a one volt increase in potential:  $C = \frac{q}{V}$ . Differentiating with respect to time gives:  $V \frac{\partial C}{\partial t} + C \frac{\partial V}{\partial t} = \frac{\partial q}{\partial t}$  which simplifies to  $C \cdot \nu = I_{\text{capacitive}}$  assuming the capacitance  $C$  is constant.

Since the capacitance a sensor experiences while testing a sample is difficult to determine beforehand, an optimised sensor would ensure that the Faradaic current far outweighs the capacitive current such that the capacitive current is relatively negligible. A Faradaic to capacitive ratio approaching 20:1 is ideally required before a sensing technique can be considered viable. To test the viability of linear sweep design described in this section, the capacitive current density was calculated for each scan rate, assuming a capacitance density of  $10\text{ }\mu\text{F}\cdot\text{cm}^{-2}$ , which is the expected approximate value for a double layer, and the values of  $I_{\text{Farad}}/I_{\text{capacitive}}$  are tabulated in Table 5.

Firstly, in the ranges investigated, at no point does the  $I_{\text{Farad}}/I_{\text{capacitive}}$  at the C/P analytical peak exceed 20, with the largest values resting around 2 to 3. This result reveals the general necessity of considering employing more complicated techniques than linear sweep voltammetry for electrochemical sensing in order to minimise the capacitive current and thus maximise the value of  $I_{\text{Farad}}/I_{\text{capacitive}}$  at the analytical peak. These techniques include square wave voltammetry or differential pulse voltammetry.

Secondly, an unexpected trend is revealed suggesting macro-electrodes tend to give better  $I_{\text{Farad}}/I_{\text{capacitive}}$  ratios than micro-electrodes in this design, which runs counter to the generally accepted idea that micro-electrodes typically enjoy weaker capacitive currents due to their reduced surface area. Whilst this is true for the direct detection of an electroactive analyte, in the case of the irreversible mediated reaction this is no longer axiomatic; the combined effects that the electrode radius has on the planarity of the diffusion regime coupled with the effects of the chemical step leads to the inference that macro-electrodes are to be favoured at the scan rates at which the Faradaic current best competes with the capacitive current.

Thirdly, the consideration of the capacitive current provides a counter-argument to maximising the scan rate when optimising a sensor of such a design: as seen in Figure 4, the optimal scan rate for maximising  $I_{\text{Farad}}/I_{\text{capacitive}}$  is heavily dependent on the chemical step's impact as determined from the electrode radius, analyte concentration and chemical rate constant. The smaller the electrode, the greater the analyte concentration or the faster the chemical rate constant, the faster the optimal scan rate must be in order to limit the effectiveness of the chemical step; meanwhile the larger the electrode, the smaller the analyte concentration or the slower the chemical rate constant, the slower the optimal scan rate must be in order to increase the time for the chemical reaction to occur and thus enhance its impact.

### 3.3. Semi-Circular Sweep Voltammetry: An Alternative Waveform

Simulations were performed using a semi-circular potential waveform.<sup>[40–47]</sup> The potential waveform is as described in Section 2.1.3.

Since the applied potential waveform is not linear it is possible to apply a higher than average scan rate at the potential at which the species  $C$  is detected whilst a relatively slower scan rate is applied at the potential of the  $A/B$  couple, allowing the generation of  $C$  from  $B$  and  $X$  to be increased and optimised. Thus, the purpose of this investigation was to reveal to what extent one might be able to enhance the analytical C/P peak current while suppressing the relative  $A/B$  peak current using this alternative waveform. As well as controlling the waveshape this can also be done by setting the value of  $\theta_{\text{shift}}$  to be closer to the C/P peak than the  $A/B$  peak. Consideration is given to how this might affect the  $I_{\text{Farad}}/I_{\text{capacitive}}$  value, which describes the ratio between the Faradaic signal current and the capacitive background current, at the C/P peak.

The position of the  $\theta_{\text{shift}}$ , as used in Equation (22), relative to the  $A/B$  and C/P peaks is vital to determining the Faradaic enhancement relative to triangular sweep voltammetry. As can be seen from Figure 6, in which voltammograms with semi-circular waveforms and varying  $\theta_{\text{shift}}$  values are super-imposed on the triangular sweep voltammogram with the same  $\sigma_{\text{avg}}$ , an

**Table 5.** Tabulation of the values of  $I_{Farad}/I_{capacitive}$  at the analytical C/P peak for the system involving a linear sweep voltammetric waveform and the titrant adsorbed to the electrode surface. Four parameters of interest are varied within the limits of physical feasibility: the analyte concentration, the electrode radius, the chemical rate constant and the scan rate. Values of  $10^6 \text{ s}^{-1}$  and  $1 \text{ cm} \cdot \text{s}^{-1}$  were chosen for  $k_0$  and  $k'_0$  respectively, both alpha values are chosen to be 0.5, the formal peak separation is set as 257 mV (which corresponds to 10 units in dimensionless theta), the diffusion coefficients of all species in solution is  $10^{-9} \text{ m}^2 \cdot \text{s}^{-1}$ , the initial surface concentration of A is  $10^{-6} \text{ mol} \cdot \text{m}^{-2}$ , and the capacitance of the electrode surface is  $10 \text{ } \mu\text{F} \cdot \text{cm}^{-2}$ . The entry N/A is given to simulations in which no analytical C/P peak is distinguishable.

[X] [ $\mu\text{M}$ ]	$\log(k_c^{\text{Het}}) [\text{M}^{-1} \cdot \text{s}^{-1}]$	$\nu [\text{mV} \cdot \text{s}^{-1}]$	$r_e = 1 \text{ } \mu\text{m}$	$r_e = 10 \text{ } \mu\text{m}$	$r_e = 100 \text{ } \mu\text{m}$	$r_e = 1000 \text{ } \mu\text{m}$
100	3	2	< 0.01	0.02	0.25	1.69
		20	0.90	1.05	1.96	3.06
		200	0.40	0.45	0.65	0.74
		2000	0.05	0.06	0.08	0.08
	6	2	< 0.01	0.01	0.12	1.14
		20	< 0.01	0.04	0.54	1.85
		200	0.01	0.18	1.45	2.30
		2000	0.07	0.91	2.69	3.10
	9	2	< 0.01	< 0.01	0.08	0.88
		20	< 0.01	0.02	0.36	1.50
		200	< 0.01	0.11	1.05	1.87
		2000	0.03	0.48	1.78	2.15
10	3	2	0.89	0.96	1.36	2.61
		20	0.39	0.41	0.53	0.68
		200	0.05	0.05	0.07	0.08
		2000	< 0.01	< 0.01	< 0.01	< 0.01
	6	2	< 0.01	0.01	0.15	1.28
		20	< 0.01	0.05	0.68	2.16
		200	0.02	0.36	2.13	1.88
		2000	1.22	0.83	0.60	0.57
	9	2	< 0.01	< 0.01	0.09	0.96
		20	< 0.01	0.03	0.42	1.66
		200	0.01	0.14	2.27	1.94
		2000	0.05	0.99	0.64	0.60
1	3	2	0.39	0.40	0.43	0.54
		20	0.05	0.05	0.06	0.07
		200	< 0.01	< 0.01	< 0.01	< 0.01
		2000	N/A	N/A	N/A	N/A
	6	2	< 0.01	0.02	0.22	2.25
		20	< 0.01	0.16	0.97	0.63
		200	1.16	0.54	0.22	0.19
		2000	0.24	0.09	0.06	0.06
	9	2	< 0.01	< 0.01	0.12	2.27
		20	< 0.01	0.04	0.99	0.64
		200	0.02	0.61	0.23	0.19
		2000	0.51	0.10	0.06	0.06

enhancement of the Faradaic C/P peak current is achievable. The closer to the C/P peak the  $\theta_{\text{shift}}$  is, the greater the C/P enhancement, as expected from causing a larger scan rate at that point in the waveform.

However, care must be taken when selecting the  $\theta_{\text{shift}}$  value to use when employing this waveform, as an "artificial" peak is induced at the  $\theta_{\text{shift}}$  point as the scan rate becomes theoretically instantaneously infinite. As seen for  $\theta_{\text{shift}} = -13$  in Figure 6, this artificial peak may obscure that of the C/P couple if  $|\theta_{\text{peak, (C/P)}} - \theta_{\text{shift}}|$  is insufficiently large. Note that for simulated voltammograms, this artificial peak height is limited by the temporal resolution one affords the simulation; for experiments, this peak height is limited by the capabilities of the potentiostat used.<sup>[43]</sup>

Consideration is next given to setting the  $\theta_{\text{shift}}$  value such that  $\theta_{f, (C/P)} < \theta_{\text{shift}} < \theta_{f, (A/B)}$ ; these  $\theta_{\text{shift}}$  values are henceforth named as intermediary  $\theta_{\text{shift}}$  values. As can be seen for  $\theta_{\text{shift}} = -7$  in Figure 6, this can produce a larger enhancement of the Faradaic C/P peak current than values of  $\theta_{\text{shift}}$  for which  $\theta_{\text{shift}} < \theta_{f, (C/P)}$ . However, simulations using intermediary  $\theta_{\text{shift}}$  values are not further investigated in this paper, as such a sensor design is

considered impractical. Intermediary  $\theta_{\text{shift}}$  values cause an excessively large enhancement of the Faradaic A/B peak, which will restrict a sensor's detection limit by obscuring the C/P peak at lower analyte concentrations. An intermediary  $\theta_{\text{shift}}$  value also requires a large and known separation in the formal potentials of the two electrochemical couples, which greatly limits the practicability and relevance of such a design.

The amplitude of the waveform is also a significant parameter when optimising the semi-circular waveform in order to maximise the Faradaic C/P peak current and suppress the Faradaic A/B peak current. Figure 7 illustrates the effect of amplitude on the voltammograms for  $k_0 = 10^6 \text{ s}^{-1}$ ,  $k_c^{\text{Het}} = 10^6 \text{ M}^{-1} \cdot \text{s}^{-1}$ ,  $k'_0 = 1 \text{ cm} \cdot \text{s}^{-1}$ ,  $\Gamma_{\text{max}} = 10^{-6} \text{ mol} \cdot \text{m}^{-2}$ ,  $\theta_{f, (C/P)} = -10$  (which corresponds to a dimensional difference in formal potentials of 257 mV),  $D_i = 10^{-9} \text{ m}^2 \cdot \text{s}^{-1}$  for all species,  $r_e = 1 \text{ mm}$ ,  $c_X^* = 0.1 \text{ mM}$ ,  $\nu_{\text{avg}} = 2 \text{ V} \cdot \text{s}^{-1}$ , and  $\theta_{\text{shift}} = -12$ . Figure 7 reveals that increasing amplitude increases the Faradaic peak current for the A/B and C/P peak. The A/B peak displays a greater amplitude-dependence than the C/P peak, as illustrated in Figure 8, which compares the peak dimensionless flux of electrons for each peak. The A/B peak



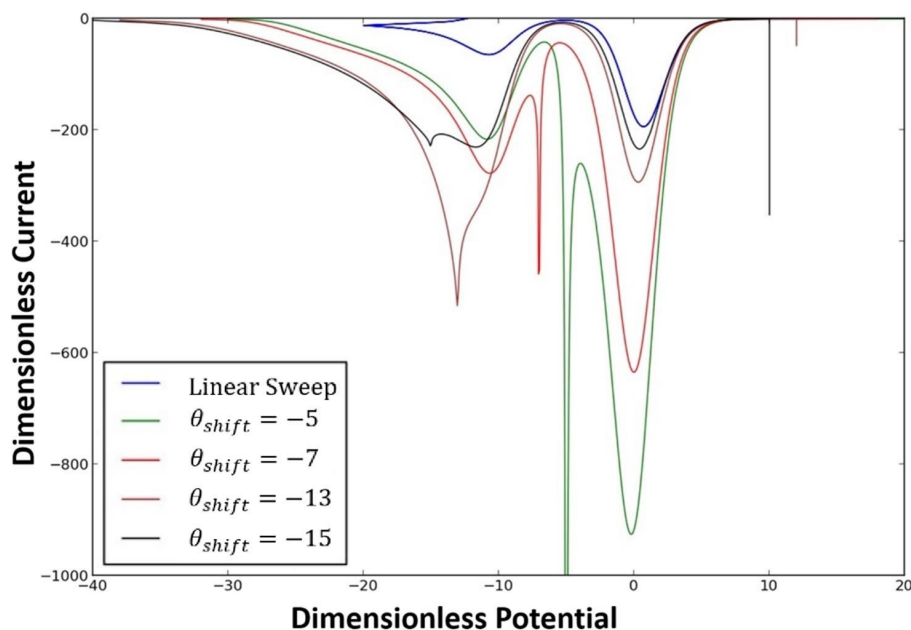


**Figure 6.** Voltammograms with a semi-circular potential waveform and titrant adsorbed to the electrode surface. The simulations were performed with the following set parameters:  $k_0 = 10^6 \text{ s}^{-1}$ ,  $k_c^{\text{het}} = 10^6 \text{ M}^{-1} \bullet \text{s}^{-1}$ ,  $k_0 = 1 \text{ cm} \cdot \text{s}^{-1}$ ,  $\Gamma_{\text{max}} = 10^6 \text{ mol} \cdot \text{m}^{-2}$ ,  $\theta_{\text{C/P}} = -10$  (which corresponds to a dimensional difference in formal potentials of 257 mV),  $D_i = 10^{-9} \text{ m}^2 \bullet \text{s}^{-1}$  for all species,  $r_e = 1 \text{ mm}$ ,  $c_x = 0.1 \text{ mM}$ ,  $v_{\text{avg}} = 2 \text{ V} \cdot \text{s}^{-1}$ , and  $A = 25$ .  $\theta_{\text{shift}}$  values between  $-5$  and  $-15$  were explored. Included in blue is the linear sweep voltammogram under the same parameters illustrated for comparison; a scan rate of  $2 \text{ V} \cdot \text{s}^{-1}$  was used for the linear sweep waveform. Only Faradaic contributions to the current have been simulated and presented in this figure.

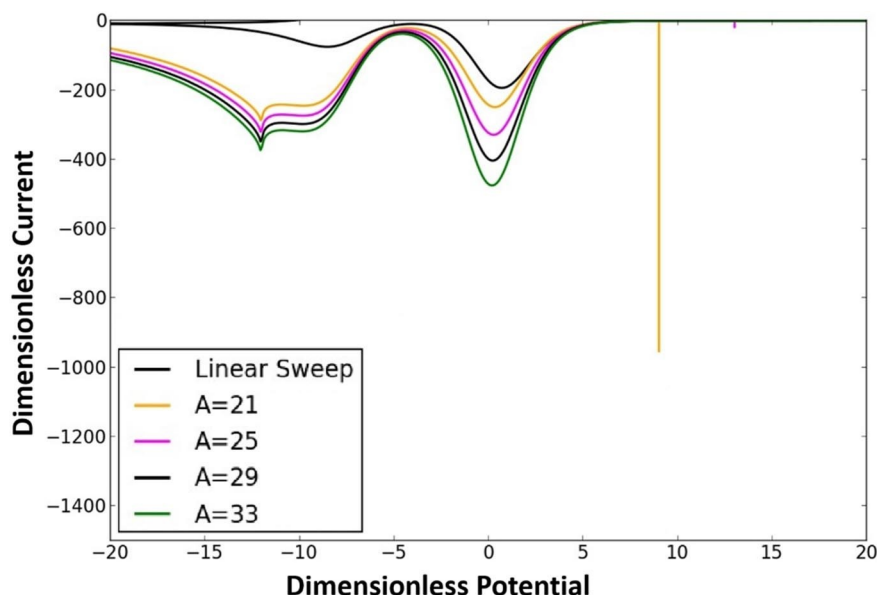


**Figure 7.** Voltammograms with a semi-circular potential waveform and titrant adsorbed to the electrode surface. The simulations were performed with the following set parameters:  $k_0 = 10^6 \text{ s}^{-1}$ ,  $k_c^{\text{het}} = 10^6 \text{ M}^{-1} \bullet \text{s}^{-1}$ ,  $k_0 = 1 \text{ cm} \cdot \text{s}^{-1}$ ,  $\Gamma_{\text{max}} = 10^6 \text{ mol} \cdot \text{m}^{-2}$ ,  $\theta_{\text{C/P}} = -10$  (which corresponds to a dimensional difference in formal potentials of 257 mV),  $D_i = 10^{-9} \text{ m}^2 \bullet \text{s}^{-1}$  for all species,  $r_e = 1 \text{ mm}$ ,  $c_x = 0.1 \text{ mM}$ ,  $v_{\text{avg}} = 2 \text{ V} \cdot \text{s}^{-1}$ , and  $\theta_{\text{shift}} = -12$ . Amplitude values between 21 and 33 are explored. Included in black is the linear sweep voltammogram under the same parameters illustrated for comparison; a scan rate of  $2 \text{ V} \cdot \text{s}^{-1}$  was used for the linear sweep waveform. Only Faradaic contributions to the current have been simulated and presented in this figure.

current and the C/P peak current both display a linear amplitude-dependence at higher amplitudes. Both peak currents deviate from this linearity at smaller amplitudes, most notably C/P, reflecting the starting potential being such that significant  $A \rightarrow B$  reduction can occur, thus complicating the

trend as the voltammogram gains some chronoamperometric-like behaviour.

Differentiation of Equation (23) with respect to  $T$  for  $c = 0$  and substitution of  $T = \sqrt{\frac{A^2 - (\theta - \theta_{\text{shift}})^2}{\sigma_{\text{avg}}^2}}$  gives the following

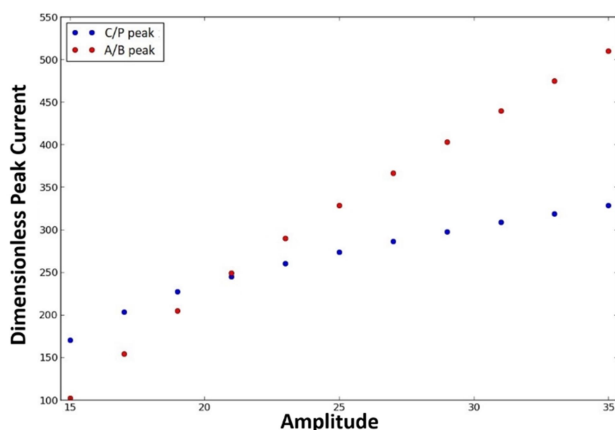


**Figure 8.** Plot of peak Faradaic current against amplitude under the parameters described for Figure 7 revealing the difference in amplitude-dependence between the A/B peak (red) and the C/P peak (blue).

equation for the dimensionless absolute scan rate during the first half of this waveform:

$$|\sigma| = \left| \frac{\partial \theta}{\partial T} \right| = \frac{|\sigma_{\text{avg}}| \sqrt{A^2 - (\theta - \theta_{\text{shift}})^2}}{\theta - \theta_{\text{shift}}} \quad (26)$$

and differentiation of Equation (26) with respect to  $A$  gives Equation (26), which reveals that, for  $\theta - \theta_{\text{shift}} > 0$ , which is the case for C/P peaks occurring at more positive potentials than the  $\theta_{\text{shift}}$ , increasing the amplitude of the waveform increases the absolute scan rate at all shared  $\theta$  values [Eq. (27)].

$$\frac{\partial |\sigma|}{\partial A} = \frac{|\sigma_{\text{avg}}| A}{\theta - \theta_{\text{shift}} \sqrt{A^2 - (\theta - \theta_{\text{shift}})^2}} \quad (27)$$

This ubiquitous increase in scan rate with the waveform's amplitude causes the increase in both Faradaic peak currents. The greater amplitude-dependence of the A/B peak is the result of the A/B peak's greater dependence on scan rate as  $J_{\text{peak}}(\text{A/B}) \propto \sigma^1$  while  $J_{\text{peak}}(\text{C/P}) \propto \sigma^{0.5}$  for a macroelectrode, or  $J_{\text{peak}}(\text{C/P}) \propto \sigma^0$  for a micro-electrode. However this relationship is complicated by the amplitude-dependence of  $\sigma$  being itself

dependent on  $\theta - \theta_{\text{shift}}$ , which is greater for the A/B peak than the C/P peak, as well as on the  $\sigma_{\text{avg}}$  and the amplitude itself.

We have seen that the Faradaic C/P peak current can be enhanced relative to the Faradaic A/B peak and optimised by variation of  $\theta_{\text{shift}}$  and  $A$ . With  $\theta_{\text{shift}}$  occurring at more negative potentials than the Faradaic C/P peak, one can expect a Faradaic enhancement of approximately 3–4 times. However, as with the triangular sweep, comparison of the Faradaic current to the capacitive current is of key importance for determining the utility of the semi-circular waveform for this design.

The capacitive current induced by the semi-circular waveform is complicated by the transient nature of the scan rate during the sweep. The capacitive current's dependence on the instantaneous scan rate, which itself relies on the waveform's  $\theta_{\text{shift}}$  and amplitude, introduces greater complexity in this regard relative to triangular sweep voltammetry.

Figure 9 illustrates how the capacitive current varies during a scan assuming constant capacitance and how this is affected by the amplitude of the waveform.

Of first note is that the fast scan rate close to the  $\theta_{\text{shift}}$  value induces a correspondingly large capacitive current which dominates the Faradaic current in this region. As a result of this, a larger  $|\theta_{\text{peak, (C/P)}} - \theta_{\text{shift}}|$  is required in order to avoid obscuring the Faradaic C/P peak's contribution to the total current than was concluded when only Faradaic considerations were taken into account, highlighting the need to consider capacitive currents, especially when proposing waveforms alternate to the traditional linear sweep. This justifies our consideration of  $\theta_{\text{shift}} = -18$  for a  $\theta_{\text{f, (C/P)}} = -7.79$ , which corresponds to a  $\theta$ -difference of 10.2 units or 260 mV, in order for the total current at  $\theta_{\text{shift}}$  to not obscure the analytical C/P peak.

Table 6 presents the values of  $I_{\text{Farad}}/I_{\text{capacitive}}$  extracted from the peak induced by the C/P couple in the Faradaic current for simulations utilising  $k_0 = 10^6 \text{ s}^{-1}$ ,  $k_c^{\text{Het}} = 10^6 \text{ M}^{-1} \cdot \text{s}^{-1}$ ,  $k'_0 = 1 \text{ cm} \cdot \text{s}^{-1}$ ,  $\Gamma_{\text{max}} = 10^{-6} \text{ mol} \cdot \text{m}^{-2}$ ,  $\theta_{\text{f, (C/P)}} = -7.788$  (which corresponds to a dimensional difference in formal potentials of 200 mV),  $D_i = 10^{-9} \text{ m}^2 \cdot \text{s}^{-1}$  for all species,  $c_x^* = 0.1 \text{ mM}$ ,  $\theta_{\text{shift}} = -18$ , and a constant capacitance of  $10 \mu\text{F} \cdot \text{cm}^{-2}$ . The point in the voltammogram from which the  $I_{\text{Farad}}/I_{\text{capacitive}}$  is extracted is chosen to be based on the Faradaic current so that values can be acquired for systems in which the Faradaic contribution is so obscured by the capacitive contribu-

**Table 6.**  $I_{\text{Farad}}/I_{\text{capacitive}}$  values extracted at the Faradaic peak current induced by the C/P couple for varying waveform amplitudes,  $v_{\text{avg}}$  and  $r_e$ . The following parameters were used for the simulations:  $k_0 = 10^6 \text{ s}^{-1}$ ,  $k_c^{\text{Het}} = 10^6 \text{ M}^{-1} \cdot \text{s}^{-1}$ ,  $k'_0 = 1 \text{ cm} \cdot \text{s}^{-1}$ ,  $\Gamma_{\text{max}} = 10^{-6} \text{ mol} \cdot \text{m}^{-2}$ ,  $\theta_{\text{f, (C/P)}} = -7.788$  (which corresponds to a dimensional difference in formal potentials of 200 mV),  $D_i = 10^{-9} \text{ m}^2 \cdot \text{s}^{-1}$  for all species,  $c_x = 0.1 \text{ mM}$ , and  $\theta_{\text{shift}} = -18$ . A constant capacitance of  $10 \mu\text{F} \cdot \text{cm}^{-2}$  is simulated.

Amplitude	$r_e = 1 \text{ mm},$ $v = 2 \text{ V} \cdot \text{s}^{-1}$	$r_e = 1 \text{ mm},$ $v = 0.2 \text{ V} \cdot \text{s}^{-1}$	$r_e = 1 \mu\text{m},$ $v = 2 \text{ V} \cdot \text{s}^{-1}$	$r_e = 1 \mu\text{m},$ $v = 0.2 \text{ V} \cdot \text{s}^{-1}$
21	2.09801	1.3824	0.03252	0.00403
25	2.50513	1.57339	0.07288	0.00680
29	2.49538	1.77123	0.13357	0.01017
33	2.40068	1.86706	0.21592	0.01276
37	2.29461	1.93064	0.31163	0.01484
41	2.19336	1.97937	0.41215	0.01671
45	2.09941	2.02032	0.51081	0.01847
49	2.01592	2.05426	0.60277	0.02015
53	1.93805	2.08568	0.68532	0.02177

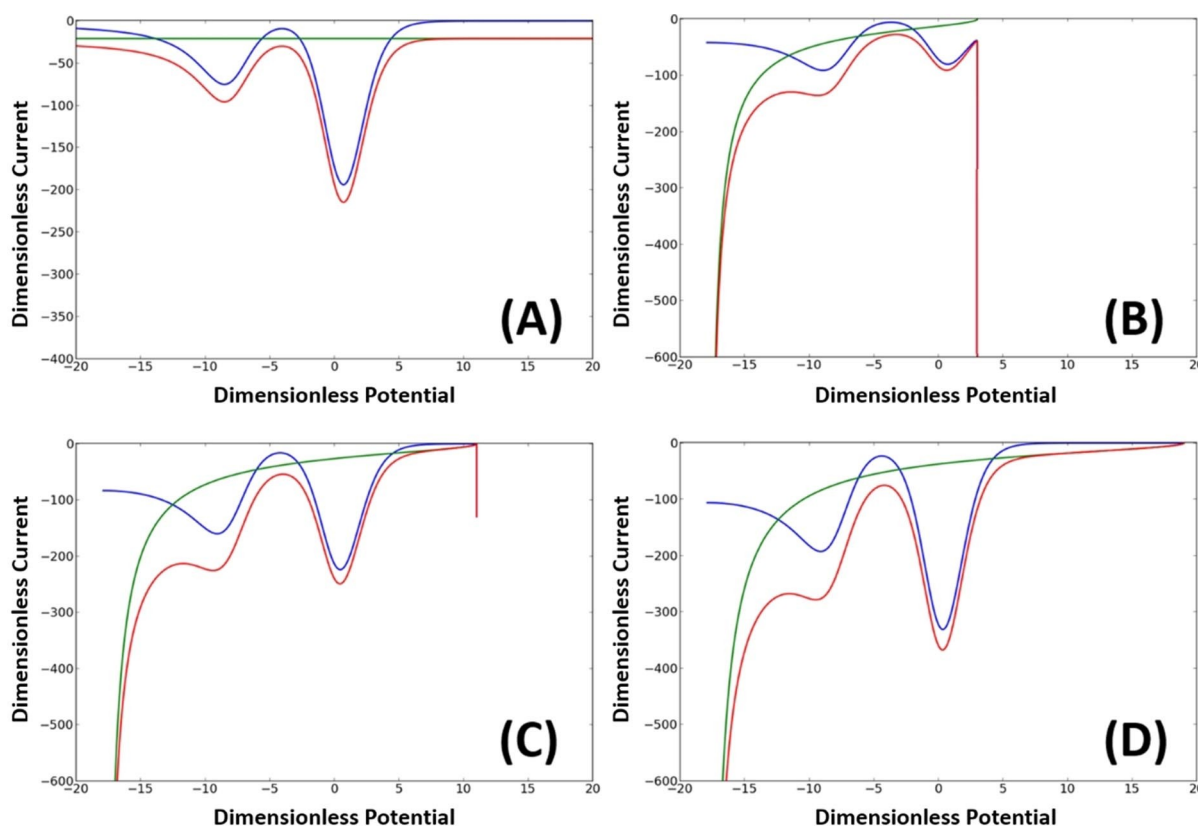


**Figure 9.** Illustration of the relative contributions of Faradaic and capacitive dimensionless currents to the total dimensionless current in voltammograms with the titrant species adsorbed to the electrode surface and utilising: **A)** a linear sweep; **B)** a semi-circular sweep with  $A = 21$ ; **C)** a semi-circular sweep with  $A = 29$ ; **D)** a semi-circular sweep with  $A = 37$ . The blue line describes the Faradaic dimensionless current, the green line describes the capacitive dimensionless current and the red line describes the total dimensionless current. The simulations were performed with the following set parameters:  $k_0 = 10^6 \text{ s}^{-1}$ ,  $k_{\text{het}} = 10^6 \text{ M}^{-1} \cdot \text{s}^{-1}$ ,  $k'_0 = 1 \text{ cm} \cdot \text{s}^{-1}$ ,  $\Gamma_{\text{max}} = 10^{-6} \text{ mol} \cdot \text{m}^{-2}$ ,  $\theta_{\text{f}, (\text{C/P})} = -7.79$  (which corresponds to a dimensional difference in formal potentials of 200 mV),  $D_i = 10^{-9} \text{ m}^2 \cdot \text{s}^{-1}$  for all species,  $r_e = 1 \text{ mm}$ ,  $C_x^* = 0.1 \text{ mM}$ ,  $v_{\text{avg}} = 2 \text{ V} \cdot \text{s}^{-1}$ , and for the semi-circular sweeps:  $\theta_{\text{shift}} = -18$ . A constant capacitance of  $10 \mu\text{F} \cdot \text{cm}^{-2}$  is simulated.

tion that the C/P peak is indistinguishable in the total current, as observed when smaller waveform amplitudes are used with the  $1 \mu\text{m}$  radius electrode system, whose  $I_{\text{Farad}}/I_{\text{capacitive}}$  values are very low. As the waveform amplitude is varied, a maximum in the extracted  $I_{\text{Farad}}/I_{\text{capacitive}}$  is observed. It is expected that increasing the amplitude, and thus increasing the scan rate in the potential-region of interest, would result in a decreasing  $I_{\text{Farad}}/I_{\text{capacitive}}$  as the capacitive current displays a first-order scan rate dependence, while the Faradaic current displays a square root dependence on a macro-electrode or zero dependence on a micro-electrode (at quasi-steady-state). However, it seems that this competes with amelioratory effects of increasing the scan rate on the Faradaic current, observed and discussed in a previous section, and that results in the appearance of this maximum. It can be seen that reducing the average scan rate or the electrode radius greatly increases the amplitude at which this maximum is observed; simulations using amplitudes up to 101 have been performed for the ( $r_e = 1 \text{ mm}$ ,  $v = 0.2 \text{ V} \cdot \text{s}^{-1}$ ) system and the ( $r_e = 1 \mu\text{m}$ ,  $v = 2 \text{ V} \cdot \text{s}^{-1}$ ) system but a maximum for either system has not been observed.

We see that the capacitive current gives a greater relative contribution to the total current than the Faradaic at the C/P peak when using a semi-circular sweep as opposed to the

corresponding linear sweep. As illustrated in Table 6, the use of a semi-circular waveform does not markedly improve the value of  $I_{\text{Farad}}/I_{\text{capacitive}}$  observed at the C/P peak relative to the linear sweep waveform. As such, though the semi-circular waveform improves the utility of the sensor design from purely Faradaic considerations, it does not help to solve the issue of the capacitance limiting the accuracy of a reading.

One suggestion for resolving this problem in a practical sensor would be to fit the curve describing the capacitive current from a semi-circular sweep to data acquired early in the sweep at very positive potentials, during which only the capacitive current contributes to the total current, and using this measurement to calculate a capacitance for the sensor-sample system. This could then be used to extrapolate and then subtract the capacitive background from the current response in the region of the C/P peak, thus improving the sensor's accuracy with a simple calculation, rather than requiring an additional experiment to determine the system's capacitance. However, we do not recommend the general use of this technique as it does not consider the likely potential-dependence of the system's capacitance. Moreover, it extends the scan-time of the sensor by requiring a larger amplitude in order to acquire data for fitting the capacitive curve.

## 4. Conclusions

In this work, a general method for the design of mediated electron-transfer sensors has been developed via numerical simulation. Models have been developed and simulations performed for the cases of titrant in solution and titrant adsorbed to the electrode surface with triangular potential waveforms. Qualitatively similar features are observed for both models: fast mediating chemical reaction rates shift the  $A/B$  couple towards irreversibility and more positive potentials and cause a secondary voltammetric peak to arise from the  $C/P$  couple. The “solution titrant” model gives greater currents than the “adsorbed titrant” model and greater sensitivity of the  $C/P$  peak current to analyte concentration. However, for reasons of detection limit and practicality, it is concluded that it is preferable to introduce the titrant species to the sample as an adsorbed monolayer on the electrode surface, as opposed to dissolving the material into the sample solution beforehand.

Optimisation of the “adsorbed titrant” design’s  $C/P$  peak current reveals that the optimal electrode radius is analyte concentration dependent such that smaller electrode radii are preferred by smaller analyte concentrations. Under the conditions simulated, micro-electrodes begin to become favoured at the micro-molar level. Optimisation also reveals the existence of an optimal rate constant for the chemical titration reaction. Consideration of the Faradaic to capacitive current ratio at the  $C/P$  peak shows that macro-electrodes are preferred over micro-electrodes for scan rates at which the Faradaic current best competes with the capacitive current for designs seeking to maximise this signal to background ratio. The competition of the Faradaic current with the capacitive current results in an optimal scan rate; the scan rate is maximised in an optimal sensor when only Faradaic current contributions are considered, with the caveat that the *normalised* Faradaic current retains an optimal scan rate.

Semi-circular potential waveforms are shown to produce an enhancement of the Faradaic current at the  $C/P$  peak relative to both triangular waveforms and relative to the  $A/B$  peak current. The optimal position of the  $\theta_{shift}$  is shown to be at a more negative potential than the  $C/P$  peak and as close to the  $C/P$  peak as possible before the spike in the capacitive current caused by the waveform obscures the  $C/P$  peak. Both Faradaic peaks increase with the waveform’s amplitude and develop linear dependencies at high amplitudes, with the  $A/B$  peak being the more sensitive. Variation of the waveform amplitude produces a maximum in the Faradaic to capacitive current ratio, the reasons for which correspond to those responsible for the maximum observed for varying scan rate with a triangular potential waveform.

Generally low values are observed for the ratio of Faradaic to capacitive current for both triangular and semi-circular sweep voltammetry. Alternative waveshapes, such as differential pulse or square wave potential waveforms, designed to reduce the effect of the capacitive current on the voltammetry are expected to greatly improve this ratio and thus the efficacy of this sensor design. Finally, we note that modelling provides a valuable complement to the development of electrochemical

sensors not least in identifying competing chemical and physical factors controlling sensitivity and limits of detection and providing a coherent framework for otherwise typically empirically approached pursuits.

## Conflict of Interest

The authors declare no conflict of interest.

**Keywords:** mediated electron transfer · sensors · semi-circular sweep · voltammetry · capacitance.

- [1] C. Brett, A. M. O. Brett, *Electroanalysis*, Oxford University Press, 1998.
- [2] C. Brett, A. M. O. Brett, *Electrochemistry: Principles, Methods, and Applications*, Oxford University Press, 1993.
- [3] H. Ju, X. Zhang, J. Wang, *NanoBiosensing: Principles, Development and Application*, Springer Science & Business Media, 2011.
- [4] X. Zhang, H. Ju, J. Wang, *Electrochemical Sensors, Biosensors and Their Biomedical Applications*, Academic Press, 2011.
- [5] K. Di Gleria, H. A. O. Hill, *Inorg. Chim. Acta* **1992**, *198*, 863–866.
- [6] G. Davis, I. Higgins, H. Hill, *J. Biomed. Eng.* **1984**, *6*, 174–175.
- [7] L. Xiong, R. G. Compton, *Int. J. Electrochem. Sci.* **2014**, *9*, 7152–7181.
- [8] Zimmer and Peacock Ltd, can be found under [www.zimmerpeacock.com](http://www.zimmerpeacock.com), 2020.
- [9] Honeywell International, can be found under <https://www.honeywellanalytics.com>, 2020.
- [10] Alphasense, can be found under <http://www.alphasense.com/>, 2020.
- [11] Mettler Toledo, can be found under <https://www.mt.com/gb/en/home.html>, 2020.
- [12] C. R. Ispas, G. Crivat, S. Andreescu, *Anal. Lett.* **2012**, *45*, 168–186.
- [13] V. Scognamiglio, G. Pezzotti, I. Pezzotti, J. Cano, K. Buonasera, D. Giannini, M. T. Giardi, *Microchim. Acta* **2010**, *170*, 215–225.
- [14] M. I. Prodromidis, M. I. Karayannis, *Electroanalysis* **2002**, *14*, 241–261.
- [15] K. Chaisiwamongkhon, C. Batchelor-McAuley, R. G. Compton, *Analyst* **2019**, *144*, 1386–1393.
- [16] K. Chaisiwamongkhon, C. Batchelor-McAuley, R. G. Compton, *Analyst* **2017**, *142*, 2828–2835.
- [17] ANB Sensors, can be found under <http://www.anbsensors.com/>, 2020.
- [18] K. Aoki, J. Osteryoung, *J. Electroanal. Chem.* **1981**, *122*, 19–35.
- [19] D. Shoup, A. Szabo, *J. Electroanal. Chem.* **1982**, *140*, 237–245.
- [20] S. Coen, D. K. Cope, D. E. Tallman, *J. Electroanal. Chem.* **1986**, *215*, 29–48.
- [21] F. Cottrell, *Z. phys. Chem.* **1903**, *42*, 385–431.
- [22] V. G. Levich, *Physicochemical Hydrodynamics*, Englewood Cliffs, N. J., Prentice-Hall, 1962.
- [23] J. K. Novev, R. G. Compton, *Curr. Opin. Electrochem.* **2018**, *7*, 118–129.
- [24] X. Li, C. Batchelor-McAuley, J. K. Novev, R. G. Compton, *Phys. Chem. Chem. Phys.* **2018**, *20*, 11794–11804.
- [25] R. G. Compton, C. E. Banks, *Understanding voltammetry*, third edition, World Scientific Press, 2018.
- [26] E. E. Tanner, R. G. Compton, *Electroanalysis* **2018**, *30*, 1336–1341.
- [27] B. R. Kozub, N. V. Rees, R. G. Compton, *Sens. Actuators B* **2010**, *143*, 539–546.
- [28] D. S. Silvester, *Curr. Opin. Electrochem.* **2019**, *15*, 7–17.
- [29] P. Jeroschewski, K. Haase, A. Trommer, P. Gründler, *Electroanalysis* **1994**, *6*, 769–772.
- [30] E. R. Lowe, C. E. Banks, R. G. Compton, *Anal. Bioanal. Chem.* **2005**, *383*, 523–531.
- [31] A. Goodwin, C. E. Banks, R. G. Compton, *Electroanalysis* **2006**, *18*, 1063–1067.
- [32] R. W. Murray, *Acc. Chem. Res.* **1980**, *13*, 135–141.
- [33] R. W. Murray, *Annu. Rev. Mater. Sci.* **1984**, *14*, 145–169.
- [34] R. W. Murray, in *Electroanal. Chem.*, ed. A. J. Bard, Marcel Dekker, New York, **1984**, *13*, 191–368.
- [35] I. Svir, A. Oleinick, R. Compton, *Russ. J. Electrochem.* **2003**, *39*, 160–164.
- [36] R. G. Compton, E. Kätelhön, E. Laborda, K. R. Ward, *Understanding voltammetry: simulation of electrode processes*, second edition, World Scientific Europe, 2020.
- [37] D. Gavaghan, *J. Electroanal. Chem.* **1998**, *456*, 1–12.

- [38] E. Kätelhön, R. G. Compton, *Analyst* **2015**, *140*, 2592–2598.
- [39] C. Batchelor-McAuley, R. G. Compton, *J. Electroanal. Chem.* **2012**, *669*, 73–81.
- [40] Y. Uchida, E. Kätelhön, R. G. Compton, *J. Electroanal. Chem.* **2018**, *818*, 140–148.
- [41] Y. Uchida, E. Kätelhön, R. G. Compton, *J. Electroanal. Chem.* **2019**, *848*, 113290.
- [42] Y. Uchida, E. Kätelhön, R. G. Compton, *J. Electroanal. Chem.* **2019**, *835*, 60–66.
- [43] H. M. Amin, Y. Uchida, E. Kätelhön, R. G. Compton, *J. Electroanal. Chem.* **2019**, *836*, 62–67.
- [44] Y. Uchida, E. Kätelhön, R. G. Compton, *J. Electroanal. Chem.* **2017**, *801*, 381–387.
- [45] Y. Uchida, E. Kätelhön, R. G. Compton, *J. Electroanal. Chem.* **2018**, *823*, 465–473.
- [46] H. Amin, Y. Uchida, C. Batchelor-McAuley, E. Kätelhön, R. G. Compton, *J. Electroanal. Chem.* **2018**, *815*, 24–29.
- [47] Y. Uchida, E. Kätelhön, R. G. Compton, *J. Electroanal. Chem.* **2018**, *810*, 135–144.
- Manuscript received: May 12, 2020  
Revised manuscript received: June 14, 2020  
Accepted manuscript online: June 15, 2020
-